

NEAR-INFRARED PROPERTIES OF MODERATE-REDSHIFT GALAXY CLUSTERS: LUMINOSITY FUNCTIONS AND DENSITY PROFILES

ADAM MUZZIN, H. K. C. YEE

adam.muzzin@utoronto.ca

Dept. of Astronomy & Astrophysics, University of Toronto
50 St. George Street, Toronto, Ontario, Canada, M5S 3H4

PATRICK B. HALL¹

phall@yorku.ca

Department of Physics & Astronomy, York University
4700 Keele Street, Toronto, Ontario, Canada, M3J 1P3

E. ELLINGSON

Erica.Ellingson@colorado.edu

Center for Astrophysics and Space Astronomy, University of Colorado at Boulder
CB389, Boulder, CO, 80309

H. LIN¹

hlin@fnal.gov

Fermi National Accelerator Laboratory
P.O. Box 500, Batavia, IL 60510

Draft version October 31, 2018

ABSTRACT

We present K-band imaging for 15 of the Canadian Network for Observational Cosmology (CNOC1) clusters. The extensive spectroscopic dataset available for these clusters allows us to determine the cluster K-band luminosity function and density profile without the need for statistical background subtraction. The luminosity density and number density profiles can be described by NFW models with concentration parameters of $c_l = 4.28 \pm 0.70$ and $c_g = 4.13 \pm 0.57$ respectively. Comparing these to the dynamical mass analysis of the same clusters shows that the galaxy luminosity and number density profiles are similar to the dark matter profile, and are not less concentrated like in local clusters. The luminosity functions show that the evolution of K* over the redshift range $0.2 < z < 0.5$ is consistent with a scenario where the majority of stars in cluster galaxies form at high-redshift ($z_f > 1.5$) and evolve passively thereafter. The best-fit for the faint-end slope of the luminosity function is $\alpha = -0.84 \pm 0.08$, which indicates that it does not evolve between $z = 0$ and $z = 0.3$. Using Principal Component Analysis of the spectra we classify cluster galaxies as either star-forming/recently-star-forming (EM+BAL) or non-starforming (ELL) and compute their respective luminosity functions. The faint-end slope of the ELL luminosity function is much shallower than for the EM+BAL galaxies at $z = 0.3$, and suggests the number of faint ELL galaxies in clusters decreases by a factor of ~ 3 from $z = 0$ to $z = 0.3$. The redshift evolution of K* for both EM+BAL and ELL types is consistent with a passively evolving stellar population formed at high-redshift. Passive evolution in both classes, as well as the total cluster luminosity function, demonstrates that the bulk of the stellar population in all bright cluster galaxies is formed at high-redshift and subsequent transformations in morphology/color/spectral-type have little effect on the total stellar mass.

Subject headings: cosmology: dark matter – large-scale structure of universe
galaxies: clusters: photometry – fundamental parameters

1. INTRODUCTION

Galaxy clusters are fundamental tools in the study of galaxy evolution because they are unique locations in the universe, where the high-density environment produces a population of galaxies that is different from the general field. The ability to predict how and when cluster galaxies are assembled, and their subsequent evolution

is an important test for any model of galaxy formation. Unfortunately, the cluster population transforms significantly in morphology, color, and star-formation properties over the redshift range $0 < z < 0.5$ and thus far, our understanding of this evolution is incomplete. At low redshift ($z < 0.2$), clusters are primarily composed of a population of quiescent early-type galaxies which obey a tight color-magnitude relation (CMR, e.g., Bower et al. 1992; Lopez-Cruz et al. 2004), morphology-density relation (Dressler 1980; Goto et al. 2003a), and spectral type-density relation (Tanaka et al. 2004; Gomez et al. 2003; Lewis et al. 2002).

¹ Visiting Astronomer, Kitt Peak National Observatory, National Optical Astronomy Observatory, which is operated by the Association of Universities for Research in Astronomy, Inc. (AURA) under cooperative agreement with the National Science Foundation.

At higher redshifts ($0.2 < z < 0.5$) the cluster galaxy population is no longer completely dominated by early-types. The number of blue galaxies in clusters increases (the Butcher-Oemler effect, e.g., Butcher & Oemler 1984; Ellingson et al. 2001; Andreon et al. 2004) and the morphological mix of galaxies also changes as the proportion of spiral galaxies increases at the expense of the early-type (primarily S0) population (e.g., Dressler et al. 1997; Postman et al. 2005; Smith et al. 2005). Despite these major changes in star-formation properties and morphology, studies of the fundamental plane (e.g., van Dokkum et al. 1998; van Dokkum & Stanford 2003; Holden et al. 2005) and the CMR (e.g., Stanford et al. 1998; Gladders et al. 1998; Holden et al. 2004) of early-type galaxies (both of which include S0 galaxies) show that their stellar populations are extremely old and consistent with a passively evolving population formed at high redshift ($z_f > 2-3$). The differences in the star-formation history of cluster galaxies and the average age of their stellar populations could be reconciled by postulating that the predecessors of low-redshift early-types are high-redshift late-types which form the bulk of their stars at high-redshift (van Dokkum et al. 2001). If transformations in color and morphology are primarily passive (i.e., from the truncation of star formation by strangulation; e.g., Balogh et al. 1999; Abraham et al. 1996; Treu et al. 2003; Goto et al. 2003b) then they should leave little imprint on the overall stellar population. The prediction that the majority of evolution in cluster galaxies from $z \sim 0.5$ to the present is simply the passive transformation of late-type galaxies into early-type galaxies is in good qualitative agreement with the data; however, it is possibly too simplistic a picture.

Recent work suggests that galaxy-galaxy mergers may play a significant role in driving cluster galaxy evolution at high redshift. Lin et al. (2004, hereafter L04) compared the Halo Occupation Distribution (HOD), the number of galaxies in a dark matter halo of a given mass) of $0.2 < z < 0.9$ clusters to that of $z < 0.1$ clusters and showed that it is *larger* by a factor of ~ 2 in the high-redshift clusters. This result implies that numerous mergers or tidal disruptions in the cluster environment at moderate to high redshift are required to reduce the number of bright cluster galaxies, and match the local HOD. The prediction of a large merger fraction is consistent with observations of MS1054-03 at $z = 0.83$ by Tran et al. (2005) and van Dokkum et al. (1999) who show that 16% of the cluster galaxies are currently undergoing major mergers. Understanding how the merger rate interplays with the transformation in color, spectral-type, and morphological-type of the cluster population without significantly altering the overall stellar population remains a challenge.

The K-band luminosity function (LF) of clusters at this redshift can provide useful information on this problem. K-band light suffers little contamination from recent star formation and dust; furthermore, the K-corrections are small, negative, and nearly independent of galaxy type (e.g., Poggianti 1997; Mannucci et al. 2001). These advantageous properties mean that K-band light is closely related to the total stellar mass of a galaxy (Brinchmann & Ellis 2000; Rix & Rieke 1993) and therefore, the K-band LF is nearly analogous to the galaxy stellar mass function. The dependence on the stellar mass contained

in galaxies makes the K-band LF a useful check on the merger rate, because its evolution will proceed quite differently depending on the number of major mergers. Furthermore, the K-band LF is also sensitive to the age of the stellar populations in cluster galaxies because it puts constraints on luminosity evolution of the stellar population. Most commonly, luminosity functions are fit to a Schechter (1976) function of the form:

$$\phi(K) = (0.4 \ln 10) \phi_* (10^{0.4(K^* - K)})^{1+\alpha} \exp(-10^{0.4(K^* - K)}), \quad (1)$$

where α is the faint-end slope; ϕ_* , the normalization; and K^* is the ‘‘characteristic’’ magnitude, which indicates the transition between the power-law behavior of the faint-end and the exponential behavior of the bright-end.

The advent of the 2 Micron All-Sky Survey (2MASS, Skrutskie et al. 2006) has facilitated a considerable number of studies of the Near Infrared (NIR) LF of clusters in the local universe (i.e., $z < 0.1$) using a very homogeneous set of data. These studies now provide a crucial comparison sample for higher-redshift NIR cluster LFs. Balogh et al. (2001, hereafter B01), Kochanek et al. (2003), Lin et al. (2003), L04, Rines et al. (2004, hereafter R04) and Ramella et al. (2004) have all investigated the K-band LF of local clusters and groups using 2MASS data. The LFs vary somewhat from sample to sample; however, it appears that the overall shape of the K-band LF in local clusters is similar to the local field. The only notable difference being that K^* is slightly ($\sim 0.2 - 0.4$ magnitudes) brighter in clusters, and K^* in groups is closer to, if not equal, the field value (Ramella et al. 2004; L04).

At higher redshift, the K-band LF of clusters is not as well constrained. Thus far, the best measurement of the evolution of the cluster K-band LF comes from the study of de Propris et al. (1999, hereafter dP99). Using a heterogeneous set of 38 clusters with $0.1 < z < 1.0$, they show that the brightening of K^* with increasing redshift is consistent with a passively evolving stellar population with a formation redshift (z_f) of $\sim 2-3$. Subsequent measurements of the K-band LF in a handful of $z > 1$ clusters have been made (Kodama & Bower 2003; Ellis & Jones 2004; Toft et al. 2004; Strazzullo et al. 2006) and those data further confirm the passive evolution scenario. The interpretation of these results has been that the majority of the stellar mass in bright cluster galaxies is already assembled into IR-bright (and therefore massive) galaxies by $z \sim 1$. It is difficult to reconcile these data with the prediction of a significant number of mergers in the cluster environment.

We have obtained wide-field K-band imaging for 15 of the 16 CNOC1 clusters (Yee et al. 1996a) to a depth of $\sim K^* + 2$. With these data we examine the redshift evolution of the K-band cluster LF, the difference between the field and cluster LFs, the LFs of clusters of different mass, and the K-band luminosity and number density profile of clusters at $0.19 < z < 0.54$ using a homogeneous, X-ray-selected cluster sample. We have IR-imaging and spectroscopy to $R \sim 1.5R_{200}$ for most clusters and this radial coverage allows us to compute the LFs for the entire virialized region without the need for statistical background subtraction. Furthermore, the spectroscopy also allows us to classify the galaxies into star-forming, and non-star-forming types and determine

how the LFs of these classes differ.

This paper is the first in a series of three which examine the NIR properties of moderate redshift clusters. The HOD, mass-to-light ratios and correlation between the cluster physical properties and K-band luminosity/richness are presented in Muzzin et al. (2006, hereafter Paper II). The evolution of the color-magnitude relation and the K-band selected Butcher-Oemler effect will be presented in a third paper (Yee et al. in-prep, hereafter Paper III).

The structure of this paper is as follows: In §2 we describe our observations, and in §3 the data reduction and calibration. Section 4 discusses the weighting scheme based on the spectroscopic catalogue that is used to construct both the density profiles and luminosity functions. In §5 we compute the K-band luminosity and number density profile of the clusters and compare with the dark matter profile. In §6 we determine the cluster K-band LF for all cluster galaxies as a function of redshift and cluster mass and compare to field LFs in the literature. In §7 we divide the galaxies into two spectral classes and show the dependence of these LFs on redshift and cluster mass. We conclude with a summary in §8. When computing magnitudes and angular sizes we adopt an $\Omega_m = 0.3$, $\Omega_\Lambda = 0.7$, $H_0 = 70 \text{ km s}^{-1} \text{ Mpc}^{-1}$ cosmology. All magnitudes quoted throughout the paper are on the Vega system.

2. OBSERVATIONS

The CNOC1 clusters are an X-ray selected sample of 16 intermediate ($0.19 < z < 0.54$) redshift clusters (Yee et al. 1996a), and are likely the most well-studied clusters in this redshift range. The masses (Carlberg et al. 1996, Borgani et al. 1999), mass-profiles (Carlberg et al. 1997a, 1997b; van der Marel et al. 2000), X-ray temperatures (Mushotzky & Scharf 1997; Henry 2000; Lewis et al. 1999; Hicks et al. 2006), X-ray luminosities (Ellis & Jones 2002), richnesses (Yee & Ellingson 2003), and stellar populations (Abraham et al. 1996; Balogh et al. 1999; Diaferio et al. 2001; Ellingson et al. 2001) have all been examined in detail. For our sample we selected 15 of the 16 CNOC1 clusters for K-band imaging. The cluster MS0906+11 was not observed because it is shown to be a strong binary in redshift-space by Carlberg et al. (1996) and therefore the cluster dynamical mass measurement is unreliable.

2.1. Optical Photometry and Spectroscopy

Gunn g and r band imaging data were obtained at the 3.6m Canada-France-Hawaii-Telescope (CFHT) as part of the original CNOC1 project (Yee et al. 1996a) using the Multi-Object Spectrograph (MOS) camera in imaging mode. The 5σ depth of the optical photometry varies from cluster-to-cluster but is typically 23.7 - 24.3 mag in g , and 23.5 - 24.0 mag in r . The CNOC1 project also acquired > 2500 spectroscopic redshifts in the fields of the 15 clusters. The spectroscopy was obtained using 1-10 masks of ~ 100 slits per cluster. Of the 2500 redshifts, approximately half are cluster members. The spectroscopic catalogues were chosen as an r -band magnitude-limited, complete sample, but are sparsely sampled. The spectroscopic magnitude limits are $r = 20.5$, 21.5, and 22.0 for clusters at $z < 0.3$, $0.3 < z < 0.45$, and $z > 0.45$ respectively. Using the passive evo-

lution color-redshift model for an early-type galaxy from Kodama et al. (1998), these spectroscopic completeness limits correspond to K-band limits of ~ 17.0 , 17.5, and 18.0 mag for the same redshift bins. The definition of the completeness limiting magnitude is that all galaxies brighter than the limit, *that had slits placed on them*, have reliably determined redshifts. However, the sparse sampling means that not all galaxies in the field brighter than the completeness limit had slits placed on them. Therefore, use of the redshift catalogues requires a selection function that corrects for the sparse sampling of the data (§4).

Complete details of the optical observations, reductions, photometry and redshift determination of these data can be found in Yee et al. (1996a). Our analysis is based on the original photometric and spectroscopic catalogues (Ellingson et al. 1998, 1997; Abraham et al. 1998; Yee et al. 1998, 1996b) and additional unpublished spectroscopy for $z < 0.3$ clusters.

2.2. Near Infrared Observations

K-band imaging for 14 of the 15 clusters was obtained at the Kitt Peak National Observatory (KPNO) 2.1m telescope using the Ohio State / NOAO Infrared Imaging Spectrograph (ONIS). The ONIS detector is a 1024×1024 InSb array with 2 working quadrants which makes it effectively a 1024×512 imager with a pixel scale of $0''.288/\text{pixel}$. The observations were made on UT 1999 February 3-4 and 1999 June 3, and were taken in a Mauna Kea Observatory filter set version of the K_s filter (Tokunaga et al. 2002), which is nearly identical to the 2MASS K_s filter. Hereafter we treat them as identical and refer to the filter simply as the “K-band”. All three nights were photometric and standard stars were observed at different airmasses for photometric calibration. The seeing in the images is typically around $1''.0$, but ranges from $0''.8$ to $1''.2$. Because of time constraints, we were unable to obtain data for one cluster (MS0440+02) during the February run. K-band imaging of MS0440+02 was instead obtained using the PISCES camera on the KPNO 2.5m telescope on UT 1999 February 27 during an imaging run for CNOC2 fields. The PISCES camera is a 1024×1024 HAWAII array with a pixel scale of $0''.495/\text{pixel}$. The PISCES imaging was done using the K_s filter. Table 1 summarizes our observational data.

2.3. Pointing Strategy and Field Coverage

The goal of the original CNOC1 observations was to obtain photometry and spectroscopic redshifts of cluster members beyond the cluster virial radius (R_{vir}), in order to determine the cluster dynamical mass-to-light ratio. For the massive, lower-redshift clusters, the angular size of R_{vir} was larger than the CFHT-MOS Field-of-View (FOV) ($\sim 10' \times 10'$) and several MOS pointings were required. For these clusters, either a north-south or east-west strip through the cluster center was observed. Column 8 of Table 1 lists the configuration of the MOS pointings. The first number in the column is the number of east-west pointings and the second is the number of north-south pointings. A 1×1 pointing is the cluster center. Column 9 lists what percentage of the area of a circle with radius R_{200} , the radius at which the mean density of the cluster exceeds the critical density by a factor of 200 (see Paper II for updated values of R_{200}

for the CNO1 clusters using a Λ CDM cosmology), is covered by the optical imaging data. Column 3 of Table 1 lists the number of cluster members (see Carlberg et al. 1996 for membership criteria) with spectroscopic redshifts within R_{200} .

In order to overlap as much of the optical imaging and spectroscopic data as possible, we designed a pointing strategy for the ONIS observations based on the locations of the CFHT MOS fields. To obtain images with similar coverage as the $\sim 10' \times 10'$ CFHT MOS (although only $\sim 8' \times 8'$ are useful for photometry and spectroscopy due to a significant radial distortion and vignetting) using the $\sim 2.5' \times 5'$ FOV of ONIS we used a 3×2 pointing pattern for each MOS field. This gives us an ONIS mosaic with a FOV of $\sim 7.5' \times 7.5'$, which is similar to the usable portion of the MOS. Each pointing consists of ~ 4 dithers of $\sim 6''$ to $10''$, and each dither consists of 1-3 internal coadds with exposure times of 25-45 seconds. The nature of the mosaicking is such that there is significant overlap of the pointings in the north-south direction and a strip in the center of each field has a higher signal-to-noise than the rest of the mosaic. The depth of the images at the lower signal-to-noise parts still reaches the limit of the spectroscopic observations, so we make no correction for the slightly uneven depth of the images. The PISCES camera has a FOV of $8' \times 8'$, nearly the same size as the MOS, and therefore we made a single PISCES pointing for each MOS pointing in MS0440+02. The PISCES pointings consist of 5 dithers of $\sim 5''$ with a 40 second exposure time.

3. DATA REDUCTION

Reduction of the ONIS data was done using the IRAF packages PHIIRS and PHAT (see Hall, Green, & Cohen, 1998). Reduction of the PISCES data was done with a modified version of the ipipe reduction package (Gilbank et al., 2003). Both of these packages employ the standard techniques for reducing NIR imaging, and here we summarize only the most important steps in the process.

The first step in the reduction is to make a first-pass dark subtraction, flat-fielding, and sky estimate for all frames. Frames are then registered and coadded into a first-pass mosaic of the cluster. Object finding is performed on this mosaic, and from this an “object mask” is made. Flat-fielding and sky subtraction are then redone using only pixels that do not appear in the the object mask. This step ensures that faint galaxies not detected in a single frame do not cause the sky level to be overestimated.

All ONIS images are flattened with dome flats (for the PISCES images we use the value of the sky itself to flat-field). Whenever possible, sky subtraction is done using a “running sky”. This procedure involves calculating the sky from a fixed number of frames taken before and after the frame for which the sky is being subtracted. Determining the sky from a small number of frames improves the photometric accuracy of the data because the moderate-duration sky variations (of the order 10 minutes in the NIR) can be removed accurately. Unfortunately, using a small number of frames to compute the sky also results in a larger Root-Mean-Squared (RMS) background in the final mosaic because shot noise is significant when using only a few frames. Our criteria for choosing the best number of frames for sky subtraction

was as follows: The sky was first computed using all the frames from a cluster (we termed this a “quick sky”). The quick sky was subtracted from all frames, and the final mosaic made. The RMS noise and standard deviation of that image are then recorded. We then repeat sky subtraction using the running sky technique. The final sky we adopt is the one that uses the fewest number of frames and gets an RMS background for the final image that is within 1σ of the quick sky image. For most clusters this results in a sky computed from ~ 16 -32 frames (i.e., approximately 5 - 10 minutes before and after each frame was observed). Once the final sky has been subtracted from each frame, we adopt an airmass extinction term of -0.08 mag for the K-band, and all frames are rescaled by $1.08 \times \langle \text{airmass} \rangle$ of the observation. As an example of the data quality, we show a portion of the final mosaics of one of the highest-redshift (MS0016+16) and lowest-redshift (Abell 2390) clusters in the sample in Figures 1 & 2.

3.1. ONIS Pattern Removal

All frames obtained using the ONIS instrument have a lined pattern that appears in the bottom-half of the image. This pattern is probably caused by extra noise generated when the camera is read out. The pattern is well-fit by a variable-amplitude sinusoid curve with a period 6 times the width of the chip. We remove the pattern by fitting each original frame (before flat-fielding and sky subtraction) with a sinusoid and then subtracting the fit from the image. In all cases the fits are good and all images are subsequently eye-checked to make sure nothing which might significantly alter the photometry is subtracted. The final mosaic for each cluster is made from the final sky-subtracted, pattern-removed frames.

3.2. PISCES Distortion Correction

The PISCES camera has a radial distortion in the focal plane. The pattern is different each time the camera is mounted on the telescope and therefore must be corrected using stars in the science images. We correct this pattern using code developed by McCarthy et al. (2001). Comparing the positions of objects on the optical images with the distortion-corrected PISCES images shows that this correction works extremely well.

3.3. Object Finding and Photometry

The g and r -band optical images are significantly deeper than the K-band images for every cluster. Therefore we match the optical catalogue positions to the K-band images using the IRAF task *xyxymatch*. The significant pincushion of the CFHT-MOS is corrected using tabulated data supplied by CFHT. In most cases this allows for excellent matches of the whole optical catalogue. In the few cases where a slight offset remains, a higher order correction is computed and then eye checked. A final eye check is made for objects that may have been so red as to be apparent only in the K-band images. Very few such objects were found (~ 1 -2 per MOS field). Those that are found are not faint Extremely Red Objects (EROs); they tend to be objects undetected in the optical image because they are obscured by the bleeding of charge from a saturated star. No attempt is made to account for these objects because there are so few.

Image not available

FIG. 1.— K-band image of the central region of MS0016+16 ($z = 0.55$), one of the highest-redshift clusters in the sample. The image has a FOV of 3.5×3.0 arcmin, and seeing of $1''.1$. North is to the top, east is to the left.

Furthermore, these galaxies do not have redshifts and therefore will have negligible impact on the results of the study.

Photometry and star-galaxy classification are done on all objects using Picture Processing Package (PPP, Yee 1991). PPP identifies objects as either stars or galaxies based on analysis of their growth curve. The r -band images are the deepest for all clusters and therefore the object classification is based exclusively on the r -band images.

Galaxy colors are nominally computed using a $3''$ diameter aperture magnitude. However, PPP determines whether this aperture is appropriate based on the object's growth curve. If the growth curve appears “normal” (i.e., it is monotonically increasing, but has a monotonically decreasing derivative) then an actual $3''$ aperture is used; however, if the growth curve is abnormal (due to, e.g., crowding from another object, or a cosmic ray hit) PPP uses the largest, non-contaminated aperture to compute the color (we refer to this diameter as the optimal aperture, d_{opt}). Computing colors using this technique is particularly useful for avoiding the crowding problems which can be significant in the dense, central parts of galaxy clusters.

Galaxy total magnitudes are determined by analyzing

the shape of the growth curve. For faint small galaxies ($r > 19$) the magnitudes are extrapolated to a diameter of $8.5''$ to account for seeing effects. The extrapolation is done using a reference Point Spread Function (PSF), determined from several bright stars in the field. For brighter galaxies ($r < 19$), variable apertures up to a maximum of $25.5''$ are used. The size of the aperture is determined from the growth curve of the object. This step is primarily employed to account for bright galaxies with large angular diameters (i.e., foreground galaxies). A thorough discussion of photometry using PPP and a comparison with simulations can be found in Yee (1991).

3.4. *Photometric Calibration and Comparison with Previous Photometry*

Photometric standards from Persson et al. (1998) were observed throughout all nights, at different airmasses. There are not enough standards to solve for the atmospheric extinction coefficient; however, comparing observations of the same standard at different air masses shows that they are consistent with -0.08 value assumed for the science frames. Standards taken throughout the night were extremely stable, so photometric zeropoints are determined for each night based on an average of all standards for that night. The standard deviations in the zeropoint calibration for the three ONIS nights are 0.022,

Image not available

FIG. 2.— K-band image of the central region of Abell 2390 ($z = 0.22$), one of the lowest-redshift clusters in the sample. The image has a FOV of $\sim 2.5 \times 3.5$ arcmin, and seeing of $1''.2$. North is to the left, east is to the bottom.

0.014, and 0.035 mag, and are determined from 3, 10, and 6 standard stars respectively. The PISCES photometric zeropoint has a standard deviation of 0.022 mag and is determined from 4 standard stars.

The cluster imaging is sufficiently wide that it contains enough bright stars per cluster field to check the consistency of the photometry with the 2MASS point-source catalogue (Skrutskie et al. 2006). The 2MASS photometric calibration is excellent, having zeropoint variations that are less than 0.02 mag across the entire survey. For the purpose of determining any differences in zeropoint, we compare the photometry of objects $13.5 < K_s < 15.0$ classified as stars by PPP in the cluster fields to the same objects in the 2MASS Point Source Catalogue. We adopt a faint limit of $K_s < 15.0$ because the mean photometric uncertainty for an individual star at $K_s \sim 15$ becomes fairly large in the 2MASS catalogue (~ 0.1 mag). We choose a bright limit of $K_s > 13.5$ because stars begin to saturate at this magnitude on the ONIS detector (the PISCES potential well is slightly deeper and therefore a bright limit of $K_s = 12.5$ is adopted for MS0440+02). The number of stars available for comparison in the fields of the clusters varies from from 6 in MS1008-12 and MS1455+22 to 70 in Abell 2390. In general, the agreement between our photometry and the

2MASS photometry is good. Eight of 15 clusters have median photometric differences of < 0.05 mag, and 12 of 15 have differences of < 0.1 mag. The cluster with the largest offset is MS0016+16, which is fainter than the 2MASS photometry by 0.18 mag. We noted the possibility of light cirrus in the logbook when observing this cluster, and assume that this is the explanation for the difference in zeropoint. Table 2 lists the clusters, the number of stars, and the mean difference between our photometry and the 2MASS photometry. Although the offsets between our calibration and the 2MASS calibration are small, we have chosen to recalibrate our photometry to the 2MASS photometry, rather than use the solutions from the standard stars. This provides consistent photometric zeropoint for the entire cluster sample. Once recalibration is complete, the magnitudes of all galaxies are corrected for Galactic reddening using the dust maps of Schlegel et al. (1998).

Three of the CNOC1 clusters (MS1358+62, MS0451-03, and MS1008-12) were also observed in the study of Stanford et al. (1998, 2002; hereafter SED02). As an additional check on the consistency of our photometry, we compare the magnitudes of all galaxies brighter than the 5σ limiting depth of the shallowest observation (in all three cases our data is shallower by ~ 0.1 mag). The

top panels of Figures 3, 4, and 5 show plots which compare our total magnitudes with the SED02 total magnitudes. The solid line in the plot has a slope of unity. The bottom panel of the plots shows the residuals. Overall, the agreement between our photometry and the SED02 photometry is poor. The median offset for MS1008-12, MS1358+62, and MS0451-03 is 0.089, 0.223, and 0.305 mag respectively, with our photometry being fainter in all cases. Objects which are extreme outliers (> 1 mag) are likely to be bad matches, as we use a relatively simple matching technique.

The systematic differences in the photometry are much larger than the zeropoint uncertainties (~ 0.02 mag for 2MASS, and ~ 0.03 mag for the SED02 data) and they are also larger than the even the largest difference between our own photometric calibration and the 2MASS calibration (0.18 mag). This makes it difficult to understand the cause of the discrepancy. The data reduction procedure employed by SED02 is nearly identical to our own, and therefore it is unlikely that this causes any systematics between the datasets. The most notable difference between the SED02 datasets and our own is that the SED02 observations were done with different cameras on different telescopes: OSIRIS on KPNO 1.3m for MS1008-12, IRIM on KPNO 2.1m for MS1358+62, and IRIM on KPNO 4m for MS0451-03 whereas ours were done with the same instrument/telescope configuration. In our program, the observations for MS1008-12 and MS1358+62 were taken consecutively on February 3. If there were some systematic change during the observations (e.g., cirrus) it most likely would have affected both of these clusters, yet the photometric calibration from the standard stars matches the 2MASS calibration for both these clusters very well ($\langle \Delta m \rangle = -0.003$ and -0.039 , for MS1008-12 and MS1368+62, respectively).

It is interesting to note that the photometry for objects brighter than $K \sim 15.0$ agrees somewhat better than for objects fainter than $K \sim 15$. Given that our zeropoints are determined using stars brighter than this, it suggests that the SED02 photometry could be as consistent with the 2MASS photometry as our own, and that the relative offset is not a zeropointing problem, but may be a systematic due to the different way magnitudes are measured. The cameras used by SED02 have a much larger pixel scale than ONIS ($0''.95/\text{pixel}$, $1''.09/\text{pixel}$, $0''.65/\text{pixel}$ for OSIRIS, IRIM-2.1m, and IRIM-4m, respectively, compared to $0''.288/\text{pixel}$ for ONIS). Such a large pixel size means that the some of their observations may be significantly undersampled if the seeing was close to $1''.0$ or better. This could pose a problem because the SED02 magnitudes were measured using the FOCAS (Valdes, 1982) code, which determines magnitudes using isophotes. SED02 then correct the FOCAS magnitudes because FOCAS tends to produce total magnitudes which are too faint. It is possible that determining isophotal magnitudes using undersampled data may result in a significant scatter, because the location of the isophote is difficult to determine. We cannot be certain that this is the source of the discrepancy over such a small area; however, because we use primarily a single instrument, and our photometry agrees well with 2MASS photometry, we are confident of the photometric accuracy of our own data.

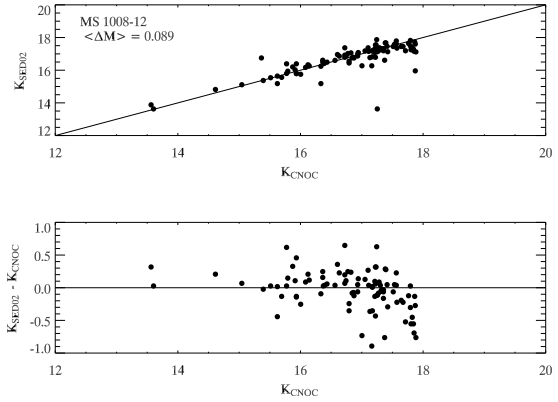


FIG. 3.— Top Panel: Total magnitudes from the SED02 photometry vs. total magnitudes from this photometry for the cluster MS1008-12. The solid line has a slope of unity and intercept of zero. Bottom Panel: Residuals from the top panel.

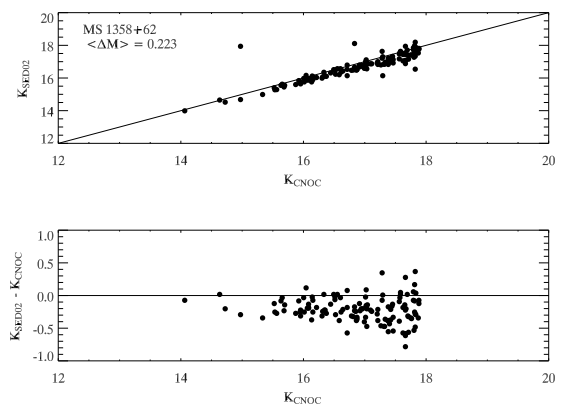


FIG. 4.— As Figure 3 for the cluster MS1358+62. Objects that are significant outliers may be poorly matched.

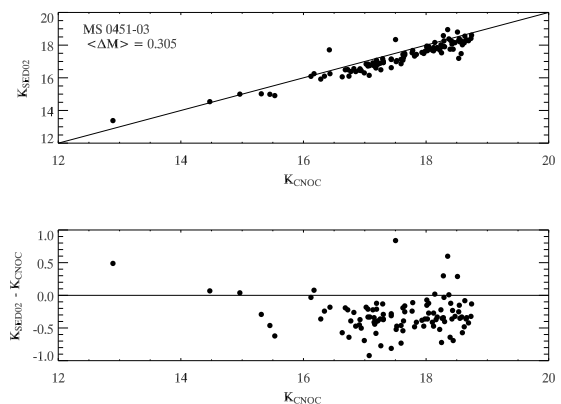


FIG. 5.— As Figure 3 for the cluster MS0451-03. Objects that are significant outliers may be poorly matched.

4. SPECTROSCOPIC SELECTION FUNCTION

The large number of spectroscopic redshifts available from the CNOC1 project allows us to measure the K-band LF and density profiles with more confidence than by statistical background subtraction; however, the cluster redshift catalogues are sparsely sampled and a weighting scheme is required to correct for the spectroscopic

selection function. Galaxies may preferentially have a measured redshift depending on their magnitude, color, position in the cluster, or z ; and the galaxy weights are a function of these four parameters.

The weighting scheme that is employed is based on the one derived by the CNOC1 and CNOC2 collaborations and is discussed thoroughly in the respective papers (Yee et al. 1996a, Yee et al. 2000). The basic philosophy behind the weighting scheme is that the distribution of galaxies with redshifts is representative of the ones without redshifts in terms of the primary selection biases. The magnitude selection function (i.e., a brighter galaxy is more likely to have a spectroscopic redshift) is overwhelmingly dominant over the other 3 possible selection effects, which can be considered “secondary effects” (Yee et al. 1996a). Incorporating the full set of weights in our computations has little effect on the final results and for simplicity of interpretation we ignore the secondary biases and use only the magnitude weights when computing the cluster LFs.

The spectroscopic weights are computed as follows. Galaxies with redshifts are compared to the total number of galaxies in running bins of ± 0.25 mag for galaxies fainter than $K^* + 1.5$, and in running bins of ± 0.50 mag for galaxies brighter than $K^* + 1.5$. K^* for each cluster is estimated using a passive evolution model (§6.3). The weight for a galaxy is then the inverse ratio of galaxies with redshifts to the total number of galaxies in its magnitude bin. The weights for the brightest cluster galaxies (BCGs) are sometimes not equal to 1, even though the spectroscopy for the BCGs is 100% complete. This occurs because there are bright field galaxies within the cluster field. In order to avoid overestimating the contribution from bright galaxies, the spectroscopic weight of the BCG in each cluster is set equal to 1.

All galaxies within the cluster field are used to compute the weights when we measure the cluster density profiles. For the LFs, only galaxies within R_{200} are used to determine the weights. We adopt this approach for the LFs because the K-band imaging does not have the same coverage as the optical imaging/spectroscopy in all clusters. A few clusters have K-band data to only $R \sim R_{200}$ whereas others have coverage well beyond R_{200} and therefore have a larger proportion of field galaxies with redshifts. Throughout the analysis in this paper, the determination of cluster membership is done using the cluster redshift-space bounds calculated by Carlberg et al. (1996).

One potentially serious problem with the spectroscopic catalogue is that it is r -band selected, yet it is being used to determine the abundance of K-band selected galaxies. If a cluster or field contains a significant number of EROs which are redder than the cluster red-sequence then they will be missing from the spectroscopic sample, and could artificially inflate the K-band spectroscopic weights. Although we already verified qualitatively that there is not a significant number of EROs in the cluster field (§3.3), one way to further confirm there is no bias in the r -band selected spectroscopic catalogue is to compare the weights computed for the r -band data to the K-band weights. Figures 6 and 7 show plots of the r -band weights and K-band weights for the clusters MS1358+62 and MS0302+16. MS1358+62 has the best spectroscopic completeness of the sample, while MS0302+16 has the

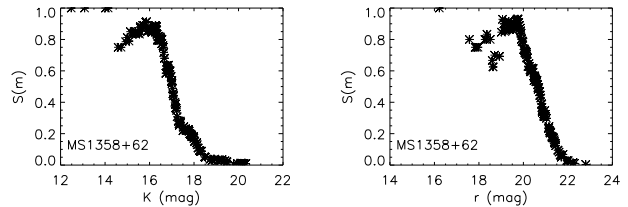


FIG. 6.— An example of the inverse of the magnitude weights ($S(m)$) for the galaxies in MS1358+62. Spectroscopic coverage of this cluster is very complete and the distribution of K-band weights is similar to the r -band weights.

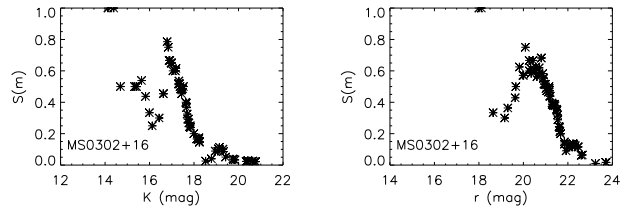


FIG. 7.— As Figure 6 for the cluster MS0302+16. Spectroscopic coverage of MS0302+16 is somewhat poor, however the distribution of K-band weights is still similar to the r -band weights.

worst. The weight functions show the characteristic dip at bright magnitudes ($r < 20$, $K < 16$) and the gradual fall-off at fainter magnitudes. The dip at bright magnitudes occurs because most of the bright galaxies are close together in the cluster core and getting slits on all of them is difficult, even with the multiple-mask strategy of CNOC1. The weight functions are similar between the K-band and r -band for both clusters, and this behavior is similar for all clusters in the sample. Therefore, we conclude that the r -selected spectroscopy is still representative of the K-band sample of galaxies.

5. CLUSTER DENSITY PROFILES

The mass density profiles and r -band number density profiles for the CNOC1 clusters have already been measured using the spectroscopic dataset by several authors (Carlberg et al. 1997a, 1997b; van der Marel et al. 2000). Here we compute the K-band selected luminosity and number density profiles as a comparison to check whether K-band selected galaxies (which better trace stellar mass) produce profiles that are different from r -selected galaxies. Computing the luminosity and number density profiles also allows us to compare the K-band density profiles of the higher-redshift CNOC1 clusters to the K-band density profiles of lower-redshift clusters (e.g., L04, R04).

The density profiles are constructed by stacking all 15 clusters into an ensemble cluster. Before adding galaxies to the ensemble cluster the radius of each cluster is normalized by its R_{200} . The number density profile is calculated by totaling the number of cluster galaxies with $K < K^* + 1$ in circular shells, scaling each galaxy by its spectroscopic weight (§4). The luminosity profile is computed in the same manner using the K-corrected, and evolution corrected (see §6.1) luminosity of galaxies with $K < K^* + 1$.

The clusters do not have homogeneous radial coverage and most are observed in a strip running through the cluster center. Therefore, the total counts or total luminosity in each shell is multiplied by the relative coverage of the shell before converting to a surface density. Some

clusters also have coverage that extends to a larger R than others. To reduce the noise at large R from poorly sampled clusters, the contribution from individual clusters is truncated at the radius where the actual coverage of the shell is less than 10% and each data point in the ensemble cluster is weighted by the number of clusters that contribute to it. The data for the ensemble cluster extends to $1.5R_{200}$.

In the top panel of Figure 8 we plot the cluster number density profile (including the BCGs) and in the bottom panel we plot the luminosity density profile (excluding the BCGs). The data are fit to a projected NFW (Navarro et al. 1997) profile of the form derived by Lokas & Mamon (2001)

$$\Sigma(R) = Ac^2 g(c) \frac{1 - |x^2 - 1|^{-1/2} C^{-1}(1/x)}{(x^2 - 1)^2}, \quad (2)$$

where c is the concentration parameter, $x \equiv R/r_s$ and

$$g(c) = [\ln(1 + c) - c/(1 + c)]^{-1}, \quad (3)$$

$$C^{-1}(x) = \begin{cases} \cos^{-1}(x) & \text{if } R > r_s \\ \cosh^{-1}(x) & \text{if } R < r_s. \end{cases} \quad (4)$$

The parameters A and c are fit using the Levenberg-Marquardt least-squares technique for χ^2 -minimization (Press et al. 1992). The best fit concentration parameter for the galaxy number density profile is $c_g = 4.13 \pm 0.57$. This agrees well with the $c_g = 3.7$ calculated by Carlberg et al. (1997b) using the r -band photometry. It is also similar to the best-fit concentration of the K-band luminosity profile, $c_l = 4.23 \pm 0.70$.

Interestingly, a good fit for the luminosity profile can only be obtained when the luminosity of the BCGs is excluded. The asterisk in the bottom panel of Figure 8 shows the value of the central point in the luminosity density with the BCGs included. This central part is better described by a power-law fit (dashed line) with an index of $n = -1.38 \pm 0.03$. The power-law can describe the luminosity profile with BCGs included approximately as well as the NFW profile does with the BCGs removed (reduced- $\chi^2 = 2.97$ and 2.79 respectively). It is perhaps surprising that the *number* density profile can be described by an NFW profile when the BCGs are included, but the *luminosity* density profile can only be fit when the BCGs are removed. This illustrates the unique nature of the BCG luminosity in the context of the formation of large-scale structure. The distribution of K-band light closely follows the distribution of K-band-selected halos throughout the cluster which suggests the average luminosity per halo is roughly constant for cluster galaxies, except the central galaxy which is by far the brightest galaxy residing in a single halo. This is also intuitively supported by the cluster LFs (§6 & §7) where the luminosity distribution of cluster galaxies is well-fit by a Schechter function, except for the BCGs which are much brighter than the rest of the population and are more abundant than a Schechter function would predict.

How do the luminosity and number density profiles compare to the cluster mass profiles? van der Marel et al. (2000) computed the mass profile of the CNOC1 clusters with detailed Jeans equation analysis. They showed that a variety of generalized density profiles fit these data well, with the best-fitting NFW model having $c_{DM} = 4.17$ (unfortunately, no error-bar is quoted for this value). This

is nearly identical to the concentration of the K-band number and luminosity density profiles and suggests that both the stellar mass contained in galaxies (excluding the BCGs) and the stellar-mass selected subhalo population, tightly trace the dark matter mass. The same conclusion was made by both Carlberg et al. (1997b) and van der Marel et al. (2000) using the r -band selected number density. However, if the BCGs are included in the luminosity profile, it appears that stellar mass may dominate over dark matter in the cluster core. The same trend is seen by Sand et al. (2004) using a sample of 6 clusters in the same redshift range ($0.17 < z < 0.44$) selected for having radial arcs. Sand et al. (2004) use a combination of strong-lensing, BCG velocity distribution and BCG luminosity to model the ratio of luminous and dark matter in cluster cores. Unfortunately, the K-band photometry and the van der Marel et al. (2000) velocity dispersion profile do not reach the resolution of the Sand et al. (2004) sample at small radii and therefore we can only remark that the CNOC1 profiles appear to be consistent with their result.

A comparison of the cluster number density profiles to those measured at lower redshift shows that the K-band light in the somewhat more massive, higher-redshift, CNOC1 clusters is more concentrated, at the 2σ level. L04 find $c_g = 2.88_{-0.10}^{+0.21}$ for an ensemble of 93 $z < 0.1$ clusters using K-band photometry from 2MASS. Similarly, R04 measure $\langle c_g \rangle = 2.83 \pm 0.56$ in the K-band for the 9 CAIRNS clusters. Unfortunately, because these samples and the CNOC1 clusters have different masses and are at different redshifts, understanding why their concentrations differ is not entirely straightforward.

N-body simulations show that c (for dark matter) is: 1) higher in lower-mass halos; 2) higher in halos which collapse first; and 3) for virialized halos becomes higher with decreasing redshift as the halo accretes mass (e.g., Navarro et al. 1997; Wechsler et al. 2002). However, the simulations show that the dependence of c on 1) and 3) is relatively weak, especially for cluster-mass halos. Given that the concentration parameter is most strongly dependent on the collapse epoch of the halo, the factor of ~ 1.5 difference between the concentrations of these samples suggests an earlier collapse time for the CNOC1 clusters. Furthermore, the fact that the CNOC1 clusters are more massive and observed at an earlier epoch than the L04 and CAIRNS clusters would seem to support this interpretation. Nonetheless, these simulations are for dark matter only, and do not measure the concentration of stellar light. Therefore, it remains possible that the difference in concentrations between the samples could be caused by a redshift evolution in the concentration of stellar light, rather than different collapse epochs for the two samples.

Interestingly, the concentration of galaxy number density and dark matter are the same in the CNOC1 clusters (within the precision of our data), yet this is not seen in the local clusters. Both L04 and R04 find that the K-band selected c_g is smaller than c_{DM} for their clusters. Their results also agree with the simulations of Nagai & Kravtsov (2005) who find $c_{DM} > c_g$ for a set of 8 clusters in a full hydrodynamical simulation. Five of the simulated clusters have c_{DM} which is a factor of ~ 2 larger than c_g , while 2 clusters have $c_{DM} \approx c_g$. The 8th cluster has $c_g > c_{DM}$. These ratios are similar to the

CAIRNS clusters, where the mean ratio between c_{DM} and c_g (for the NFW model) is 2.3 ± 0.67 . While the errors in c_g and c_l for the CNOC1 clusters are somewhat large, they still exclude the possibility that the number density of K-band-selected galaxies is less concentrated than the matter by a factor of 2 at the 3σ level ($c_g/c_{DM} = 0.99 \pm 0.14$ and $c_l/c_{DM} = 1.01 \pm 0.17$), suggesting a real difference between the moderate and low-redshift cluster samples.

If we assume that the ratio of $c_{DM}/c_g \approx 2$ at $z = 0$ seen by R04 and L04 is universal for galaxy clusters, then this suggests the possibility of an evolution in the relative c_g and c_{DM} with redshift. For c_{DM} to increase faster than c_l or c_g would require a preferential radial segregation of dark matter and light during the accretion process. One consideration is that such a segregation could be mimicked by a redshift evolution in the radial distribution of cluster galaxy stellar populations. While possible, this is unlikely to be the case for our profiles which are computed using K-band light, which is fairly insensitive to star-formation properties or dust. Furthermore, they are computed using a cut of $K < K^* + 1.0$ where K^* is very well determined and consistent with simple passive evolution (§6.3).

The simulations of Nagai & Kravtsov (2005) show that accreted galaxies near the cluster core have had $\sim 70\%$ of their total halo mass stripped since being accreted by the cluster, whereas those near the virial radius have lost only $\sim 30\%$. Since stellar mass tends to be tightly bound within a dark matter halo, the process of tidal stripping of dark matter subhalos could plausibly cause a differential evolution in c_{DM} and c_g for galaxy clusters. The tidally stripped dark matter of the infalling galaxies may sink to the center of the cluster halo and increase c_{DM} , while the stellar mass will remain bound to the subhalo and continue to orbit within the cluster halo, where it preferentially spends more time at the perimeter.

While this is a possibility, we note that with the current dataset it is impossible to untangle whether the difference in the relative concentrations of dark matter and stellar mass between the moderate and low-redshift samples is caused by such an evolution or simply because the ratio of c_{DM} to c_g is not universal for all cluster masses at all epochs. It would be interesting to compare these results with simulations that trace the redshift evolution of the cluster c_{DM} and c_g . It would also be useful to compare to simulations that have the same c_{DM} as the CNOC1 clusters. We note that all of the Nagai & Kravtsov (2005) clusters have higher concentrations than the CNOC1 clusters and that the two clusters with the lowest concentrations (which are similar to the CNOC1 clusters) have a ratio of $c_{DM}/c_g \approx 1$.

6. CLUSTER LUMINOSITY FUNCTIONS

In this section we compute the K-band LFs for cluster galaxies. Our technique for creating stacked, k-corrected LFs using clusters at different redshifts and correcting for imaging of varying depths is discussed in §6.1. The method outlined there is used to create all LFs in the remainder of the paper (§6 and §7). In §6.2 we construct an ensemble cluster LF using all 15 clusters centered at $z \sim 0.3$. This allows us to fit the faint-end slope of cluster LF (α) as well as compare it to field LFs at the same redshift. In §6.3 and §6.4 we examine the redshift evo-

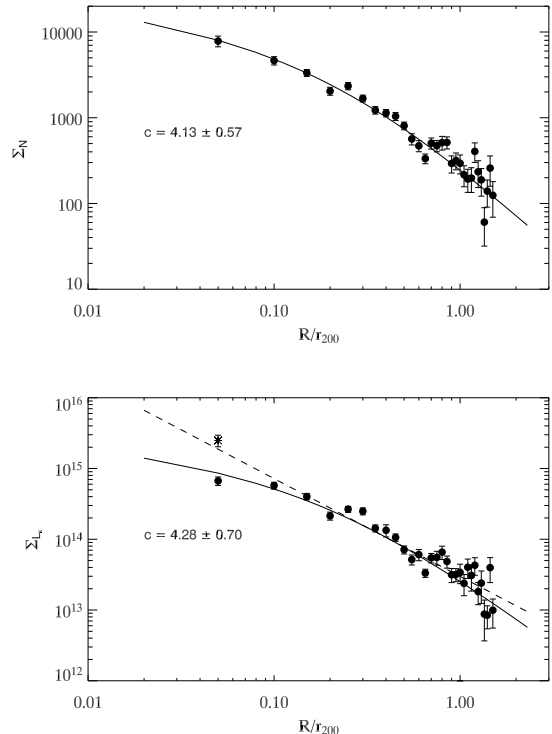


FIG. 8.— Top Panel: Surface number density per virial area of K-band selected galaxies vs. radius. The solid line is the best-fit NFW profile. Bottom Panel: Surface K-band luminosity density per virial area vs. radius. The asterisk is the luminosity density calculated when the BCGs are included. The solid line is the best-fit NFW profile excluding the BCGs. The dashed line is the best-fit power-law ($\gamma = -1.38 \pm 0.03$) including the BCGs.

lution of K^* as well as its dependence on cluster mass using a fixed value of α .

6.1. Technique for Constructing Luminosity Functions

LFs are constructed by stacking the sample of 15 clusters into either a single cluster (§6.2, §7.2) or else into 3 redshift (§6.3, §7.3) or mass (§6.4, §7.4) bins with 5 clusters per bin. Many clusters have enough spectroscopy to determine their individual LFs reasonably well; however, stacking the clusters improves the statistical errors. The LFs are constructed by counting the number of cluster galaxies (multiplied by their spectroscopic magnitude weights) within R_{200} in bins of 0.25 mag. Most clusters have some galaxies that lie outside the projected R_{200} but have velocities consistent with cluster membership; these galaxies are excluded from the LFs. R04 showed that the K-band cluster LF becomes fainter by ~ 0.5 magnitudes from the virialized to infall regions in local clusters. There is insufficient coverage of the infall region to compute a separate LF and therefore the LFs are constructed using only galaxies within the virialized region.

The cluster BCGs are not removed when computing the luminosity functions. The inclusion the BCGs results in inflated reduced- χ^2 's for the fits (because the BCGs do not follow a Schechter function); however, similar to the optical cluster LFs of de Propris et al. (2003), we find that removing the BCGs has no significant effect on the fitted value of K^* (~ 0.01 mag). Therefore, the BCGs are included as an indication of their abundance relative to other cluster galaxies. In the determination

of all LFs (§6 and §7) no attempt is made to account for the incomplete coverage of R_{200} in some clusters. Most clusters have full coverage of R_{200} , and those that do not have a strip of observations across the cluster which provides reasonably equal sampling of the cluster center and the periphery.

The clusters are at different redshifts and therefore stacking them requires that the magnitudes of galaxies within each cluster be “redshifted” to a common redshift. For the ensemble LFs (§6.2, §7.2) and the LFs for clusters of different masses (§6.4, §7.4) we use absolute magnitudes at a common redshift of $z = 0.296$, the median redshift of the sample. This requires the computation of a distance modulus, k-correction and differential evolution correction for each galaxy. When we compute the redshift evolution of the LFs (§6.3, §7.3) we keep the conventions of the literature and use apparent magnitudes. This requires only a differential distance modulus and differential k-correction.

6.1.1. *k*-Corrections

The k-corrections are taken from the models of Poggianti (1997) who list corrections for E, E1 (an early-type with longer duration episode of star-formation, which we consider an S0), Sa, and Sc types. The K-band k-corrections are fairly independent of spectral type; however, there are small differences, and therefore determining a spectral type for each galaxy is preferable. The availability of the optical photometry allows us to compute $g - r$ colors and estimate the spectral type of each galaxy using a simple model for how the colors of different spectral types evolve with redshift. We have fit the $g - r$ vs. r color-magnitude relation of each cluster (Paper III) using the biweight estimator (Beers et al. 1990). For the purpose of spectral classification of the galaxies, we assume that all cluster galaxies that are < 0.1 magnitudes bluer than the cluster red-sequence are early-type galaxies. The redshift/color models of Fukugita, Shimasaku, & Ichikawa (1995) are then used as template colors for the remaining galaxies. Rather than directly using the colors in their models, the color of an early-type galaxy at the appropriate redshift is determined empirically from the cluster color-magnitude relation, and then the *differential* colors from the models are used to determine whether galaxies are S0, Sa, or Sc types. This approach minimizes any systematics which might be caused by incorrect normalization of the models. Furthermore, because the colors between the 4 spectral types are significantly different, it implies an error of ± 1 spectral type at most. This is fairly inconsequential as the k-corrections differ by only 0.02 - 0.05 mag across all spectral-types for galaxies at $0.2 < z < 0.55$.

6.1.2. *Evolution Correction*

Previous studies have shown that there is strong luminosity evolution with redshift in the K-band for both field (Drory et al. 2003, Feulner et al. 2003, Pozzetti et al. 2003) and cluster (dP99) galaxies. Therefore, a differential evolution correction must be included in the LFs to “evolve” higher and lower redshift clusters to the appropriate redshift. We use the evolution corrections listed in Poggianti (1997). The Poggianti models consist of 15 Gyr old galaxies in a $q_0 = 0.225$, $H_0 = 50$

km s^{-1} cosmology. We have adjusted the evolution corrections by assuming the galaxies are 13.7 Gyr old at the present, and then mapped the $q_0 = 0.225$ cosmology on to our own by comparing lookback times. Once this correction is made, the Poggianti evolution corrections are in excellent agreement with our own measurement of the luminosity evolution for cluster galaxies (see §6.3). Computing the LF at the median redshift of the clusters, rather than correcting to $z = 0$ allows smaller evolution corrections (which are of order 0.08 to 0.18 mag depending on spectral-type and cluster redshift) and therefore, the choice of evolution model does not strongly affect the results from the LFs.

6.1.3. *Completeness*

Not all clusters have photometry which is complete to the same absolute magnitude; hence, to maximize the depth of the stacked LFs we adopt the approach of Schechter (1976). The clusters are ranked by limiting absolute magnitude, and the limiting magnitude of the stacked LFs is set by the depth of the deepest cluster. Clusters are then added to the stacked LF in the order of deepest to shallowest. The counts at magnitudes fainter than the completeness limit for a shallower cluster are extrapolated from the stacked LF of the deeper clusters. Using this technique means that the faintest bins in the stacked LF are scaled versions of the faint-end of the deepest clusters, whereas the bright end is determined from all clusters. While not strictly correct, it maximizes the information on the bright-end of the LF, where the statistics are poorest. Furthermore, most of the clusters are complete to approximately the same depth ($\sim K_* + 2$) with only the two highest redshift clusters (MS0016+16 and MS0451-03) being notably shallower ($\sim K_* + 1$); hence, only the faintest bins are affected by this approach. Because we do not use statistical background subtraction we assume the errors in each bin of the LF to simply be Poisson errors. The errors are computed *before* the faint-end of the LF is scaled.

The fitting of all LFs is done using the Levenberg-Marquardt algorithm for χ^2 minimization (Press et al. 1992). Errors for the parameters are estimated from the covariance matrix.

6.2. *Ensemble Luminosity Function and Comparison of the Cluster and Field Luminosity Function at Moderate Redshift*

Here we construct a composite LF from all 15 CNOC1 clusters. By stacking the clusters we reduce the statistical errors and are able to make a good measurement of both K^* and α using imaging of only moderate depth.

Figure 9 shows the composite LF for all clusters centered at $z = 0.296$, the median redshift of the sample. The best-fit Schechter function parameters are $K^* = -24.53 \pm 0.15$ and $\alpha = -0.84 \pm 0.08$. The fit parameters for this LF as well as all other LFs computed in this paper are listed in Table 3. If we compare this LF to the local K-band cluster LF measured by L04 we find the following. 1) The faint-end of the LF has not evolved from $z = 0$, to $z = 0.3$. L04 find that the best-fit α for their LF is $\alpha = -0.84 \pm 0.02$, which is identical to the best-fit for the CNOC1 clusters. 2) The evolution in K^* is consistent with a passive luminosity evolution of the stellar population. L04 measure $K^* = -24.02 \pm 0.02$ for

their clusters, which implies K^* for the CNOC1 clusters is 0.51 ± 0.15 mag brighter at $z = 0.3$. The Poggianti evolution model (adapted to our cosmology, §6.1) predicts 0.31 magnitudes of luminosity evolution from $z = 0$ to $z = 0.3$ for an early-type galaxy, which is smaller, but consistent with the observed evolution. A more detailed investigation and discussion of the redshift evolution of K^* is presented in §6.3.

The cluster LF shows no significant change (other than the passive aging of the stellar populations) with redshift between $z = 0$ and $z = 0.3$; however, it is worthwhile to consider whether it depends on environment at $z = 0.3$. In the local universe the K-band LFs of the field and cluster environments are different. B01, Lin et al. (2003), L04, R04, Ramella et al. (2004), and Kochanek et al. (2003) have all shown that the field and cluster have similar faint-end slopes, but that K^* is brighter (by $\sim 0.2 - 0.4$ mag) in clusters. Recently, several $z > 0.1$ field K-band LFs have become available in the literature, and we can now compare the cluster and field LFs at $z = 0.3$.

Pozzetti et al. (2003) use the K20 survey with a set of ~ 500 spectroscopic redshifts to determine the evolution of the K-band field LF from $z = 0.2$ to $z = 1.5$. They find that the evolution of K^* to $z \sim 1$ is consistent with a luminosity evolution of $\Delta K^* = -0.54 \pm 0.12$. The MUNICS survey group combined their K-band photometry with spectroscopic (Feulner et al. 2003) and photometric (Drory et al. 2003) redshifts to determine the evolution of the K-band field LF from $z = 0$ to $z \sim 1$. Feulner et al. (2003) find that the K-band field galaxy LF evolves by $\Delta K^* = -0.70 \pm 0.30$ magnitudes from $z = 0$ to $z \sim 1$, while Drory et al. (2003) find similar ($\Delta K^* \sim -0.5$ to -0.7 mag) results.

The faint-end slopes of the field LFs are steeper than the $\alpha = -0.84 \pm 0.08$ measured for the CNOC1 clusters. In their $z = 0.2 - 0.65$ redshift bin, Pozzetti et al. (2003) find that $\alpha = -1.25_{-0.20}^{+0.25}$, and Feulner et al. (2003) assume that $\alpha = -1.1$ in their $z = 0.1 - 0.3$ and $z = 0.3 - 0.6$ redshift bins. Unfortunately, the correlation between K^* and α makes the comparison of K^* from LFs that use different values of α difficult to interpret. Therefore, we refit the cluster LF forcing α to be fixed at -1.1 . This fit is shown as the dashed line in Figure 9. With α fixed at -1.1 , the best-fit value for the cluster LF is $K^* = -24.93 \pm 0.04$ (the smaller error bar arises because α is held fixed).

The field LFs have coarse redshift bins, and therefore we can only compare the cluster and field LFs as an average over a broad redshift range. For example, the lowest redshift bin in the Pozzetti et al. (2003) study is $0.2 < z < 0.65$, which spans the entire redshift range of the CNOC1 clusters. The mean redshift of the CNOC1 clusters is similar to the mean redshift of the two lowest bins from Feulner et al. (2003), so we average those values to $K^* = -24.68 \pm 0.26$ at $z \sim 0.3$. Comparing this to our value shows that K^* is 0.25 ± 0.26 magnitudes brighter in clusters than the field at $z \sim 0.3$. If we compare our LF to the $z = 0.2 - 0.6$ redshift bin of Pozzetti et al. (2003) who obtain $K^* = -24.87_{-0.77}^{+0.54}$ we find that K^* in clusters is $0.05_{-0.77}^{+0.54}$ magnitudes brighter than in the field. Both these values agree within the large error bars; however, the error bar on the Feulner et al. (2003) value is sig-

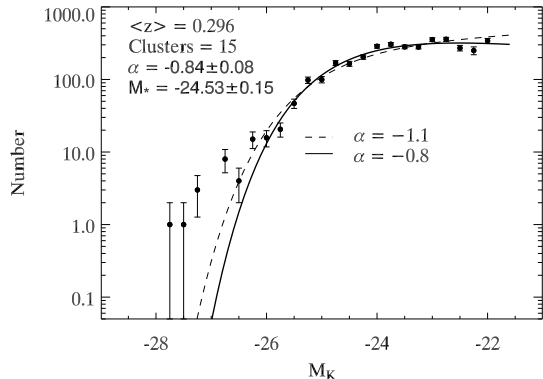


FIG. 9.— Stacked LF for all 15 clusters, corrected to a redshift of $z = 0.296$. The solid line is the best-fit Schechter function ($K^* = -24.53 \pm 0.15$, $\alpha = -0.84 \pm 0.08$). The dashed line is the best-fit Schechter function with a fixed $\alpha = -1.1$ ($K^* = -24.93 \pm 0.04$). The bright end of the LF diverges from a Schechter function because the BCGs are included.

nificantly smaller, and consistent with the results from the much larger photometric redshift study of Drory et al. (2003). Therefore, we adopt $\Delta K^* = -0.25 \pm 0.26$ between field and cluster at $z \sim 0.3$ as our best result.

Unfortunately, the errors bars on the field values of K^* are quite large, and clearly any difference between the cluster and field at moderate redshift is of the order of the error bars or less. Despite the large error bars, it is interesting to note that the difference in K^* between cluster and field galaxies at $z = 0.3$ is similar to that at $z \sim 0$. This suggests that the processes which cause the K-band luminosity function, and by corollary the stellar mass function, to be brighter in clusters (e.g., hierarchical growth of cluster galaxies from mergers) probably have already occurred by $z \sim 0.3$, and that there is little differential evolution since then. A larger field K-band study, with finer redshift bins and better constraints on K^* would be useful for investigating this further.

6.3. Redshift Evolution of the Cluster Luminosity Function

In §6.2 we showed that the composite LF for all 15 CNOC1 clusters, when compared with $z \sim 0$ clusters, is consistent with no evolution in the faint-end slope and passive evolution of the stellar populations. Here we make a more detailed examination of the redshift evolution of K^* by separating the clusters into 3 redshift bins with 5 clusters per bin. The LFs are computed at the mean redshift of the 5 clusters within each bin. This corresponds to redshift bins of $z = 0.21, 0.29$, and 0.46 . For these LFs we use apparent rather than absolute magnitudes so that we can make a direct comparison to the LFs of dP99.

When the LFs are separated into redshift bins, they do not have enough depth to obtain meaningful constraints on both K^* and α (especially in the highest redshift bin). Therefore, we hold α constant and fit only K^* and ϕ^* . Rather than assume $\alpha = -0.84$, the best-fit value for the ensemble LF, we adopt the value of $\alpha = -0.9$ assumed by dP99, which is consistent with our best-fit. Because of the strong correlation between K^* and α , assuming the same faint-end slope also allows for a straightforward comparison of K^* 's from different studies. We note that

given that there is a $\sim 10\%$ uncertainty in α from the combined LF (§6.2), the error on K^* for a given α is an underestimate of the total error budget. To obtain an estimate of the total error budget for K^* which includes the uncertainty in α , we refit the LFs with values of α that range from -0.76 to -0.92 (i.e., enclosing the 1σ error bar in α from §6.2). This refitting results in values of K^* that are +0.15 magnitudes fainter when $\alpha = 0.76$ and -0.05 magnitudes brighter when $\alpha = 0.92$. These additional deviations are comparable to the fitting errors with fixed α (see Table 3).

In Figure 10 we plot the LFs and the Schechter function fits for the 3 redshift bins. The redshift evolution of K^* for the CNOC1 clusters is compared with the dP99 values in Figure 11. The lines in the figure are models of single-burst populations with a $z_f = 1.0, 1.5, 2.0, 2.8,$ and 5.0 constructed using the Bruzual & Charlot (2003) code. The model is a 0.1 Gyr duration single-burst with solar metallicity followed by an exponentially declining star-formation rate with $\tau = 0.1$ Gyr. The model is normalized to $K^* = -24.02$ at $z = 0$, the L04 value which was measured using a faint-end slope ($\alpha = -0.84$) that is similar to the $\alpha = -0.9$ assumed for our clusters and the dP99 clusters. Figure 11 demonstrates that the stellar populations in CNOC1 clusters are consistent with a passively evolving population formed at $z > 1.5$; however, the values of K^* for the CNOC1 clusters are significantly fainter than those of the dP99 clusters. If we compare the $z = 0.21, 0.29,$ and 0.46 bins of the CNOC1 clusters to the $z = 0.20, 0.32,$ and 0.46 bins of dP99, K^* for the CNOC1 clusters is fainter by 0.36, 0.19, and 0.76 mag, respectively, and are 0.44 mag fainter on average.

We have considered several possible explanations for the very different values of K^* between the studies, the most likely of which is the systematic differences in the photometry. In §3.4 we noted that for the 3 clusters that overlap our sample and the SED02 sample (the data used to compute the dP99 LFs), our photometry is systematically fainter by 0.21 mag. If the entire datasets differ by this much, then this accounts for approximately half of the discrepancy in K^* .

It is possible that the different radial coverage in the two samples is partially responsible for the difference in K^* . R04 showed that the K-band cluster LF becomes fainter from the virial to infall region. If a such radial dependence also exists within the virial region, then this may partially explain the discrepancy because the dP99 data cover only the central region of the clusters ($\sim 0.5 - 1$ Mpc) whereas our observations cover out to R_{200} ($\sim 1 - 2$ Mpc) for most clusters. We test this possibility by recomputing the LFs using only galaxies within 0.5 Mpc of the cluster center. K^* from those luminosity functions is brighter; however, by only ~ 0.1 magnitudes, which is smaller than the discrepancy, even if photometry accounts for a portion of it. We also consider the possibility that the size of the magnitude bins used for the LFs may influence the value of K^* . dP99 use larger bins (0.5 mag) which might bias the value of K^* to brighter values because of the poor statistics at the bright-end of the LF. When we recompute our LFs using 0.5 mag bins instead of 0.25 mag bins we find that this has no effect on K^* .

Perhaps the most significant difference in the methods used to derive the luminosity functions is that we use spectroscopic redshifts, whereas dP99 use statisti-

cal background subtraction. In principle, both methods work equally well, however, the statistical method requires the stacking of a large number of clusters, because cosmic variance in the background can cause large errors in the LFs. Two of the three dP99 redshift bins that compare with ours have only a few clusters in each bin (3, 9, and 2 respectively). A higher than average background in the cluster field might result in an overestimate of the number of cluster galaxies. We cannot be conclusive as to why the value of K^* in the CNOC1 clusters is significantly fainter than in the dP99 sample; however, our simple comparisons suggest that the size of the magnitude bins and the different radial coverage between the samples has little effect on K^* . Most likely, the difference is caused by differences in the photometry (§3.4), and possibly because of the different techniques used for background subtraction.

Comparing the LFs to the $K^* = -24.02$, $\alpha = -0.84$ LF of L04 shows there is an evolution of $\Delta K^* = -0.35 \pm 0.06$ mag from $z = 0$ to $z = 0.46$. This agrees well with the passive evolution predicted from the Bruzual & Charlot single burst, $z_f = 2.8$ model ($\Delta K^* = -0.40$) and the passive evolution from the Poggianti (1997) model ($\Delta K^* = -0.39$). We conclude that the CNOC1 clusters agree well with the scenario where the bulk of the stars in galaxies are formed at high-redshift and evolve passively thereafter. Furthermore, the close relation between the K-band light and stellar mass of a galaxy suggest that the stellar mass function of $K < K^* + 2$ cluster galaxies is unchanged up to $z = 0.3$.

It is difficult to understand how no evolution in α (§6.2) and purely passive evolution of K^* is compatible with the L04 HOD data which suggest a significant number of mergers in this redshift range. Even if mergers populate all parts of the LF appropriately as to maintain the overall shape, K^* would have to be fainter than passive evolution at higher-redshift to account for the breakup of galaxies into their progenitors. It is possible that the reduction in luminosity of galaxies at high redshift due to breakup could be offset by increased amounts of star-formation which correspondingly brighten the galaxy, and therefore mimic passive evolution; however, such a scenario seems contrived, and the most reasonable interpretation of the data is that galaxies in massive, relaxed, X-ray-selected clusters do not experience a significant number of mergers between $0 < z < 0.3$. This may not be a surprising result, as the high velocity dispersion of galaxies in the cluster environment makes merging difficult. The passive evolution of the LFs at moderate redshift does not rule out the possibility that mergers play a role in cluster galaxy evolution; however, it suggests that if they are important, they most likely occur in higher-redshift systems that are in the process of relaxing (e.g., MS1054+03, Tran et al. 2005), rather than massive virialized clusters at $z \sim 0.3$.

6.4. Luminosity Functions of Different Mass Clusters

Here we separate the CNOC1 sample into 3 mass bins using cluster dynamical masses determined from the velocity dispersions of Carlberg et al. (1997a, see Paper II for values of M_{200} computed using a Λ CDM cosmology) and investigate the dependence of the K-band LF on cluster mass. The mean masses of the three bins are $\langle M_{200} \rangle = 2.73 \times 10^{14} M_\odot$, $5.96 \times 10^{14} M_\odot$, and 1.34

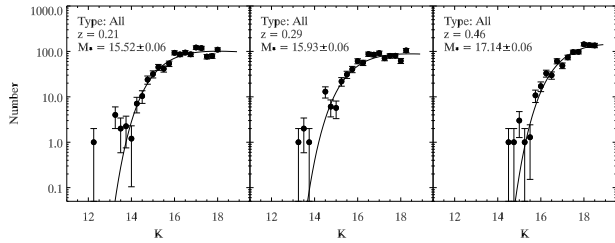


FIG. 10.— Stacked LF for clusters in three different redshift bins. Each LF is composed from a stack of 5 clusters that have been corrected to the mean redshift listed in each panel. The solid-line is the best-fit Schechter function assuming $\alpha = -0.9$. The bright-end of the LFs sometimes diverge from a Schechter function because the BCGs are included.

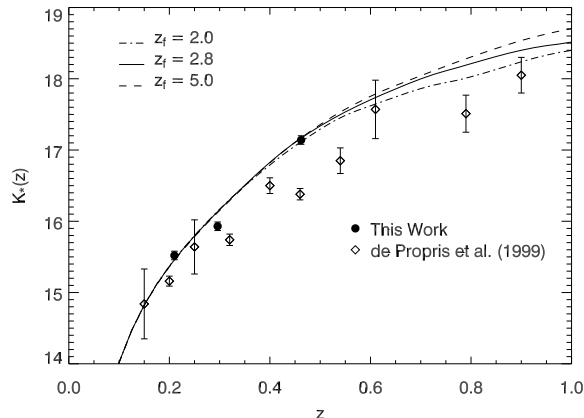


FIG. 11.— Evolution of K^* as a function of redshift. Solid points are the CNOC1 cluster LFs (Figure 10) and the open diamonds are clusters from dP99. The long-dashed, triple-dot-dashed, dot-dashed, solid, and dashed lines are single burst models with $z_f = 1.0, 1.5, 2.0, 2.8, 5.0$ respectively. The models have been normalized to the low-redshift value of K^* from the L04 study (see text). The bright galaxies in the CNOC1 clusters are consistent with a scenario where the bulk of the stellar mass is formed at high redshift and evolves passively thereafter.

$\times 10^{15} M_{\odot}$, and we designate these low, mid, and high-mass bins, respectively.

Figure 12 shows the LFs for the 3 mass bins, as well as the best Schechter function fits, again using a fixed $\alpha = -0.9$. The values of K^* for the three mass bins are $K^* = -24.51 \pm 0.08, -24.59 \pm 0.06, -24.52 \pm 0.05$ for the low, mid and high mass bins respectively. This shows that there is no significant dependence of K^* on cluster mass over the one order-of-magnitude range in mass covered by the CNOC1 clusters.

Interestingly, L04 do not find the same result in local clusters. They divide their sample of 93 clusters into high and low-mass subgroups (using masses determined from X-ray temperatures) and find that α is similar between the two groups ($\alpha = -0.84 \pm 0.03$ and -0.81 ± 0.04 for high-mass and low-mass clusters, respectively); however, K^* is brighter by 0.16 ± 0.07 mag in high-mass clusters ($K^* = -24.10 \pm 0.04$ in high-mass clusters vs. $K^* = -23.94 \pm 0.06$ in low-mass clusters). The L04 high-mass clusters have a mean M_{200} similar to the mid-mass CNOC1 clusters, while their low-mass clusters have a mean M_{200} similar to the low-mass CNOC1 clusters, and therefore the corresponding difference between those mass bins in the CNOC1 sample is $\Delta K^* = -0.08 \pm 0.10$ mag.

The dP99 clusters have a similar redshift range as the

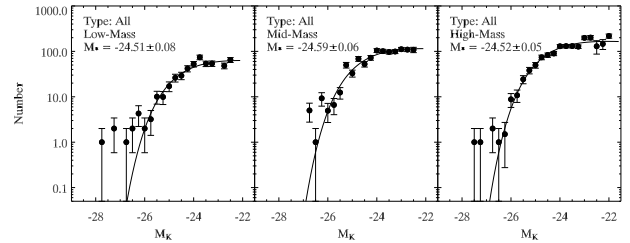


FIG. 12.— Stacked LF for clusters in three different mass bins. Each LF is composed from a stack of 5 clusters. The solid-line is the best-fit Schechter function assuming $\alpha = -0.9$. The bright-end of the LFs sometimes diverge from a Schechter function because the BCGs are included. There appears to be no correlation between K^* and mass for over the mass range covered by the CNOC1 clusters.

CNOC1 clusters, and similarly, they do not show a dependence of K^* on cluster mass. Although masses for their clusters were unavailable at the time, dP99 divided their sample into high and low optical richness and high and low X-ray luminosity (L_x) subgroups. Both optical richness and L_x are correlated with cluster mass (Yee & Ellingson 2003; although there is some scatter) and therefore these subgroups can be considered roughly as high and low-mass subgroups. Similar to our result, dP99 find that within the errors, K^* is the same between high and low richness and high and low L_x clusters from $z = 0.15$ to $z \sim 1.0$.

Given the uncertainty of our measurement of the difference in K^* between different mass bins, our result is consistent at $< 1 \sigma$ with both no dependence of K^* on cluster mass (dP99) or a very weak (~ 0.1 mag) dependence of K^* on cluster mass (L04).

7. LUMINOSITY FUNCTIONS OF DIFFERENT SPECTRAL-TYPES

The analysis in §6 demonstrated that the K-band cluster LF shows no evolution in α and only passive evolution in K^* from $z = 0$ to $z = 0.3$. Because of the close correlation between K-band light and stellar mass it also suggests no strong evolution in the stellar mass function of cluster galaxies over this redshift range. However, studies of the evolution of morphology-density relation (Postman et al. 2005, Smith et al., 2005, Dressler et al., 1997), as well as the star-formation rate in clusters (e.g., Balogh et al. 1999, Poggianti et al. 1999), and the Butcher-Oemler effect (Ellingson et al. 2001) suggest that there is significant evolution in the morphological and star-formation properties of the cluster galaxy population over the same redshift range. Therefore, it seems likely that that the LFs of the early and late-type populations will evolve differently over this redshift range, even though the combined LF of cluster galaxies shows only passive evolution.

This possibility can be addressed directly within the CNOC1 sample using the spectroscopy. Ellingson et al. (2001) performed Principal Component Analysis (PCA) on the spectroscopic data and classified galaxies into three broad spectral-types. In this section we use the PCA analysis and examine the K-band LF of these spectral-types. In §7.1 we briefly summarize the PCA decomposition. In §7.2 we construct a composite LF for the spectral types using all 15 clusters so that we can fit α . Using the best-fit values of α we study the redshift evolution of K^* and its dependence on cluster mass for the different spectral types in §7.3 and §7.4.

7.1. PCA Decomposition

Here we present a brief discussion of the PCA analysis. A thorough explanation of the fitting method and reliability of the spectral-typing is presented in Ellingson et al. (2001). The principal components of a galaxy's spectrum are determined by decomposing it using three galaxy types as eigenvectors: Elliptical, Emission-line, and Balmer-line. The template spectra used for these types are composite spectra drawn from the Las Campanas Redshift survey (Shectman et al. 1996). In the PCA analysis, each eigenvector is assigned an amplitude from 0 to 1, based on how well it represents the spectrum being fit. The total amplitude of all three eigenvectors adds up to 1. While this analysis is simplistic, it is quite effective at providing a reasonable quantitative measurement of the principal component of a galaxy's spectrum. Using the amplitudes of the PCA decomposition we divide the galaxies into 2 broad spectral-types: Early (ELL), and Emission + Balmer (EM+BAL). Galaxies with $ELL > 0.5$ are considered ELL, and those with $ELL < 0.5$ are considered part of the EM+BAL class. This provides a simple way to identify star-forming or recently star-forming galaxies from those which are dominated by absorption-lines and are likely to have been quiescent for at least a few Gyr. It is important to note that this analysis is a spectral analysis, not a morphological one. Galaxies which have early-type morphologies may still be considered EM+BAL galaxies if they show the appropriate spectral features (in fact, the BCGs in the highest redshift clusters all show emission lines and therefore do not fall into the ELL category). Separating galaxies by spectral-type (rather than morphology) is similar to the analysis done by B01 for low-redshift clusters and groups (although they use line indices, not PCA), and therefore allows easy comparison between moderate and low-redshift clusters.

7.2. Ensemble Spectrally-Types Luminosity Functions

In Figure 13 we show the LFs for ELL and EL+BAL classes. Immediately obvious is the difference between the faint-end slopes of the two LFs. The best-fit faint-end slope for the EM+BAL galaxies is $\alpha = -0.95 \pm 0.27$, while for the ELL galaxies it is $\alpha = 0.17 \pm 0.18$. This difference indicates significant redshift evolution in the faint populations of these spectral-types because in the local field and local clusters their faint-end slopes are nearly identical.

In the local field, Kochanek et al. (2001) showed that for morphologically-typed galaxies, early and late-types have faint-end slopes of -0.92 ± 0.10 and -0.87 ± 0.09 respectively. Bell et al. (2003) performed the same analysis using spectral-types from Sloan Digital Sky Survey (SDSS) spectroscopy and 2MASS photometry and found that α was similar across the types, but that it was slightly shallower for the early-types. In local clusters B01 examined a set of galaxies in the field, group, and cluster environment using 2MASS photometry and spectroscopic redshifts from the Las Campanas Redshift Survey. They split their sample into emission-line (EL) and no-emission-line (NEL) types and although the error bars are large, they find that local cluster EL and NEL galaxies have comparable faint-end slopes ($\alpha = -1.18 \pm 0.76$ for EL and $\alpha = -1.28 \pm 0.50$ for NEL). They also

find that these values of α are similar to their local field and group values for EL and NEL galaxies.

Our result suggests a strong decrease in the faint ELL population in clusters from $z = 0$ to $z = 0.3$, whereas the faint EM+BAL population remains mostly unchanged. We can make a rough estimate of the relative decrease of $K^* < K < K^* + 2$ ELL galaxies between $z = 0$ and $z = 0.3$ by integrating the LFs. Assuming the B01, $z = 0$ value of α in local clusters ($\alpha = -1.18 \pm 0.76$) and our own best-fit value for $z = 0.3$ clusters ($\alpha = 0.17 \pm 0.18$) and integrating the number of galaxies between $K^* < K < K^* + 2$ for these different values of α , we find that the number of ELL galaxies with $K^* < K < K^* + 2$ decreases by a factor of 3.8 over this redshift range. Considering the large error bar in the B01 value of α , we also compare to an $\alpha = -0.92$ LF (the Kochanek et al. 2001 value for field early-types). If the local cluster early-type population has the same faint-end slope as the field, then the relative decrease in $K^* < K < K^* + 2$ galaxies is a factor of 2.6.

One potential concern with our ELL LF is that it may suffer from selection effects caused by difficulty obtaining successful redshifts for faint, absorption-line systems. Extensive tests on the completeness of the spectroscopy (Yee et al. 1996) and PCA analysis (Ellingson et al. 2001) show that the spectroscopy is complete to the adopted limits; however, given the implications it is worth exploring this result further. As a check that the measured decrease in α is not caused by selection effects in the faintest bins, we refit the ELL LF using galaxies more than a full magnitude brighter than the spectroscopic completeness limit. This LF has a slightly steeper slope and a larger error bar ($\alpha = -0.04 \pm 0.24$); however, it is $> 3\sigma$ different than the EM+BAL limit. Furthermore, within the error, it is completely consistent with the measurement using the full spectroscopic catalogue. From this we conclude that a significant difference in the number of faint ELL vs. EM+BAL galaxies does exist, and is not a selection effect.

A decreasing number of faint, non-starforming galaxies with increasing redshift is expected in the “downsizing” scenario of galaxy formation (Cowie et al. 1996). Moreover, the same decrease is predicted by studies of the fundamental plane in the local universe. Nelan et al. (2005) show that the typical age of the stellar populations of low-luminosity early-types is ~ 4 Gyr. If these galaxies form in the monolithic collapse scenario, then this suggests that they would be star-forming galaxies at $z > 0.3$ and would not populate the faint-end of the ELL LF.

The same trend has also been observed as a decrease in the number of faint red-sequence galaxies at high redshift. Kodama et al. (2004), De Lucia et al. (2004), and Tanaka et al. (2005) all show that clusters at $z > 0.7$ have fewer faint red-sequence galaxies than their low-redshift counterparts.

Interestingly, the decrease in faint ELL galaxies in the CNOC1 clusters is not met with a corresponding increase in the number of EM+BAL galaxies. The faint-end slope measured from these galaxies is in good agreement with the local field and cluster values. This suggests that if the faint-end of the ELL LF is built-up between $z = 0.3$ and $z = 0$ from the quenching of star-formation in faint EM+BAL galaxies, that these galaxies must be replen-

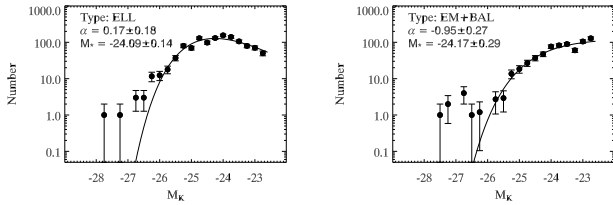


FIG. 13.— Left Panel: Ensemble LF for galaxies in all 15 clusters with spectra classified as ELL. The LF is corrected to $z = 0.296$. Right Panel: Same as the left panel for galaxies classified as EM+BAL. The bright-end of the LFs diverge from a Schechter function because the BCGs are included.

ished in order to maintain the faint-end slope. This could naturally be explained by a scenario where faint, star-forming galaxies are continuously accreted from the field and gradually transformed into quiescent galaxies.

7.3. Redshift Evolution of Spectrally-Typed Luminosity Functions

It is also useful to test whether the value of K^* from the spectrally-typed LFs shows any differential evolution with redshift. Here we compute LFs for the spectral-types at different redshifts in the identical manner as §6.3. For these LFs we hold the faint-end fixed using the values measured in §7.2 ($\alpha = 0.2$ for ELL galaxies and $\alpha = -0.9$ for EM+BAL galaxies). Figure 14 shows the resulting LFs, and the Schechter function fits. Surprisingly, the ELL LFs have fainter values of K^* than the EM+BAL galaxies. The same result is not seen in local K-band cluster and field studies. B01 show that in local clusters the NEL galaxies are 0.60 mag brighter than the EL galaxies and Kochanek et al. (2001) show that they are 0.55 mag brighter in the local field. While K^* is brighter for the EM+BAL galaxies in the CNOC1 clusters, this does not mean that the average EM+BAL galaxy is brighter than the average ELL because K^* and α are correlated. Shallower values of α typically result in fainter values of K^* . As an example, if we refit the ELL galaxies using a much steeper faint-end slope $\alpha = -0.5$ (the value measured for the stellar mass function of early-type galaxies in the local universe by Bell et al. 2003), then we find that K_* is brighter for the ELL galaxies by 0.51, 0.50, and 0.59 mag for the $z = 0.21$, 0.29, and 0.46 bins, and that, similar to the local K-band studies, the ELL galaxies have values of K_* which are brighter than the EM+BAL galaxies.

We can compare the evolution of K^* with some simple models of galaxy evolution. The left and right panels of Figure 15 shows a plot of K^* vs. z for the ELL and EM+BAL types, respectively. The solid-line in the right panel is a $z_f = 2.8$ single-burst model normalized to the B01 value of $K^* = -23.31$ for EL galaxies at $z = 0$. The dashed line in the right panel is a stellar population constructed with the Bruzual & Charlot (2003) code which forms half its stars in a single-burst at $z = 2.8$, and the other half with a constant star-formation rate of $5M_\odot \text{ yr}^{-1}$. The solid line in the left panel shows the $z_f = 2.8$ single-burst model for the ELL galaxies. Unfortunately, the ELL passive evolution model can not be normalized to the K^* computed for the NEL LF by B01 because it is measured using $\alpha = -1.28$ and this value is very different from the $\alpha = 0.2$ that we use. Instead, the ELL single-burst model is normalized to pass through the $z = 0.29$ value of K^* for ELL galaxies.

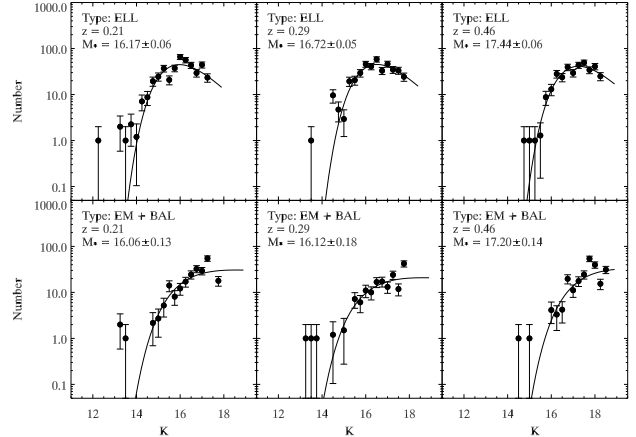


FIG. 14.— Top Row: LFs at increasing redshift for galaxies classified as ELL. Bottom Row: Luminosity functions at increasing redshift for galaxies classified as EM+BAL. Each LF is constructed from a stack of 5 clusters.

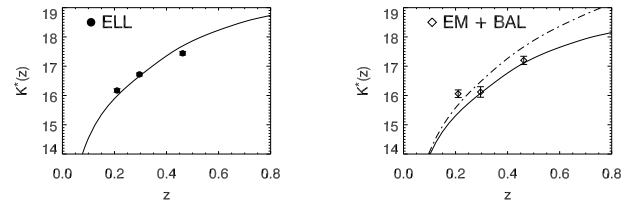


FIG. 15.— Left Panel: Redshift evolution in K^* for ELL galaxies. The solid line is passive evolution model normalized to pass through the $z = 0.29$ point. Right Panel: Redshift evolution in K^* for EM+BAL galaxies. The solid-line is a passive evolution model normalized to the B01 EL K^* . The dot-dashed line is a single-burst + constant star-formation rate model with the same normalization.

While it is difficult to make robust conclusions from Figure 15, it is worth noting that both the ELL and EM+BAL types are consistent with single-burst, passive evolution models. This result, combined with the fact that the total cluster K^* evolves passively would be consistent with a scenario where the bulk of the stellar mass in bright cluster galaxies is formed at high-redshift and the dominant evolution thereafter is the passive aging of the stellar populations, *regardless of spectral-type*. It also suggests there is no inconsistency between studies which find a significant change in the morphology, color and star-formation properties of the cluster galaxy population at $z > 0.1$, and studies which have shown that the evolution of their stellar population is primarily passive (e.g., Stanford et al. 1998, van Dokkum et al. 1998). Even though the LFs of the ELL and EM+BAL galaxies at $z = 0.3$ change significantly by $z = 0$, there is no corresponding change the total cluster LF. This suggests that the transformations in morphology and color/spectral-type which occur to cluster galaxies over the same redshift range are “superficial” - they have little effect on the overall stellar mass of the galaxies which transform.

7.4. Dependence of Spectrally-Typed Luminosity Functions on Cluster Mass

In §6.4 we showed that there was no dependence of the overall K-band LF on cluster mass for the mass range covered by the CNOC1 clusters. Here we test whether the LFs of galaxies of different spectral-types varies in

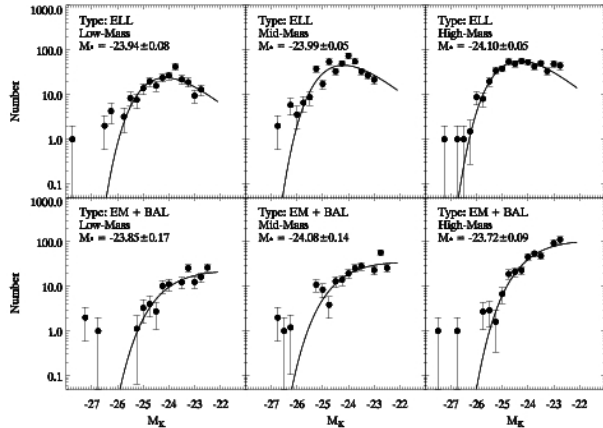


FIG. 16.— Top Row: LFs for galaxies classified as ELL in clusters of different mass. Bottom Row: Luminosity functions for galaxies classified as EM+BAL in the same clusters. Each LF is constructed from a stack of 5 clusters, and corrected to a mean redshift of $z = 0.296$

clusters of different mass.

Figure 16 shows the LFs for the ELL and EM+BAL types in the 3 mass bins used in §6.4. The LFs are computed by again assuming $\alpha = 0.2$ for ELL galaxies and $\alpha = -0.9$ for EM+BAL galaxies. Figure 16 demonstrates that there is no significant change in K^* for both spectral types across all three mass bins, with the possible exception of a slight trend (at $\sim 2\sigma$ level) with mass for the ELL galaxies. This suggests that any properties of the cluster environment that depend on the cluster mass (e.g., ram-pressure stripping efficiency, tidal forces) do not drastically alter the LF of different spectral types. It might be expected that there would be fewer faint, EM+BAL galaxies than bright EM+BAL galaxies in higher-mass clusters, as they would be more susceptible to having their star-formation truncated by tidal forces or ram-pressure stripping. However, to the depth of our LFs, we see no such reduction in the number of these galaxies.

Also, given that K^* becomes brighter through the field, group, and cluster environment in the local universe (Kochanek et al. 2001, B01, Ramella et al. 2004, L04, R04) it is surprising that there is no significant difference for the spectral-types across the cluster mass spectrum.

8. SUMMARY

We have presented K-band photometry for 15 moderate-redshift CNOC1 clusters with extensive optical spectroscopy. Our results show that both the luminosity and number density profiles of the clusters are well-fit by NFW profiles with concentration parameters of $c \sim 4$. Furthermore, comparison with the dynamical mass analysis for the same clusters shows that for massive, moderate-redshift, X-ray selected clusters, K-band light closely traces the dark matter mass at $R < 1.5R_{200}$, except possibly in the cluster core. The galaxy number and luminosity densities of the CNOC1 clusters are more concentrated than local clusters, and this is likely caused

by an earlier collapse epoch for the higher-mass, higher-redshift CNOC1 clusters. Furthermore, the ratio of c_{DM} to c_g for the CNOC1 clusters is less than in local clusters and we suggest that this is the product of either a non-universal ratio of c_{DM} to c_g for clusters, or else a relative evolution in c_{DM} and c_g with redshift.

Analysis of the cluster LFs show that the evolution of K^* between $0.2 < z < 0.5$ is consistent with a scenario where the majority of the stellar mass in cluster galaxies forms at high redshift ($z_f > 1.5$) and evolves passively thereafter. The faint-end slope of the LF shows no evolution from the value measured in local clusters. These results imply that the stellar mass buildup of individual galaxies through major mergers is negligible in massive, X-ray selected clusters from $z = 0.3$ to $z = 0$.

We have also compared the K-band luminosity functions at moderate redshift in different environments ranging from the field to high-mass clusters. Our results suggest that K^* may increase slightly in brightness from the field to the cluster environment at moderate-redshift; however, the error bars on the field K-band LFs are large and therefore, the data could also be consistent with no change. Unlike local clusters, it appears that for the CNOC1 clusters there is no correlation between K^* and the dynamical mass of the cluster.

By dividing galaxies into star-forming/recently star-forming (EM+BAL) and non-starforming (ELL) types we examined the individual LFs of these types. The faint-end slope of the ELL LF is significantly shallower than the faint-end slope for EM+BAL LF. Comparing the value of α for ELL galaxies to local field and cluster LFs suggest that the number of passive $K^* < K < K^* + 2$ galaxies in clusters decreases by a factor of ~ 3 from $z = 0$ to $z = 0.3$. These results are consistent with “downsizing” in the cluster galaxy population.

The spectrally-typed LFs also show that K^* for both ELL and EM+BAL galaxies is consistent with a passive evolution scenario and this, in tandem with the passive evolution of the combined cluster LF, suggests that the bulk of the stellar mass in both types of galaxies is formed at high-redshift, and that subsequent star-formation or changes in morphology do not affect the overall stellar mass of the galaxies. The spectrally-typed LFs also show that K^* for both EM+BAL and ELL classes is independent of the mass of the cluster that they reside in.

A.M. would like to cite useful conversations and help from David Gilbank and Kris Blindert which significantly improved the quality of the data analysis. A. M. acknowledges financial support from the National Science and Engineering Research Council (NSERC) in the form of PGSA and PGSD2 scholarships. The research of H.K.C.Y. is supported by grants from Canada Research Chair Program, NSERC and the University of Toronto. E.E. acknowledges support for this research from the National Science Foundation under Grants No. 9617145 and 0206154. P.H. acknowledges support from NSERC.

REFERENCES

Abraham, R. G., Yee, H. K. C., Ellingson, E., Carlberg, R.G., Gravel, P. 1998, ApJS, 116, 231
Abraham, R. G., et al. 1996, AJ, 471, 694

Andreon, S., Lobo, C., Iovino, A. 2004, MNRAS, 349, 889
Balogh, M. L., Christlein, D., Zabludoff, A. I., Zaritsky, D. 2001, ApJ, 557, 117

- Balogh, M., Morris, S. L., Yee, H. K. C., Carlberg, R. G., Ellingson, E. 1999, *ApJ*, 527, 54
- Beers, T. C., Flynn, K., & Gebhardt, K. 1990, *AJ*, 100, 32
- Bell, E., McIntosh, D. H., Katz, N., & Weinberg, M. D. 2003, *ApJS*, 149, 289
- Borgani, S., Girardi, M., Carlberg, R. G., Yee, H. K. C., Ellingson, E. 1999, *ApJ*, 527, 561
- Bower, R. G., Lucey, J. R., Ellis, R. S. 1992, *MNRAS*, 254, 601
- Brinchmann, J., & Ellis, R. S. 2000, *ApJ*, 536, 77
- Bruzual, G., & Charlot, S. 2003, *MNRAS*, 344, 1000
- Butcher, H., Oemler, A. J. 1984, *ApJ*, 285, 426
- Carlberg, R. G., Yee, H. K. C., Ellingson, E., Abraham R., Gravel, P., Morris, S. M., & Pritchett, C.J. 1996, *ApJ*, 462, 32
- Carlberg, R. G., Yee, H. K. C., & Ellingson, E. 1997a, *ApJ*, 478, 462
- Carlberg, R. G., et al. 1997b, *ApJ*, 485, L13
- Cowie, L. L., Songaila, A., Hu, E. M., Cohen, J. G. 1996, *AJ*, 112, 839
- De Lucia, G., et al. 2004, *ApJ*, 610, L77
- De Propris, R., et al. 2003, *MNRAS*, 342, 745
- De Propris, R., Stanford, S. A., Eisenhardt, P. R., Dickinson, M., Elston, R. 1999, *AJ*, 118, 719
- Diaferio, A. Kauffman, G., Balogh, M. L., White, S. D. M., Schade, D., Ellinson, E. 2001, *MNRAS*, 323, 999
- Dressler, A., et al. 1997, *ApJ*, 490, 577
- Dressler, A. 1980, *ApJ*, 236, 351
- Drory, N., Bender, R., Feulner, G., Hopp, U., Maraston, C., Snigula, J., Hill, G. J. 2003, *ApJ*, 595, 698
- Ellingson, E., Lin, H., Yee, H. K. C., & Carlberg, R. G. 2001, *ApJ*, 547, 609
- Ellingson, E., Yee, H. K. C., Abraham, R. G., Morris, S. L., Carlberg, R. G. 1998, *ApJS*, 116, 247
- Ellingson, E., Yee, H. K. C., Abraham, R. G., Morris, S. L., Carlberg, R. G., Smecker-Hane, T. A. 1997, *ApJS*, 113, 1
- Ellis, S., Jones, L. 2004, *Proc. IAU Coll #195, astro-ph # 0405043*
- Ellis, S. C., & Jones, L. R. 2002, *MNRAS*, 330, 631
- Feulner, G., Bender, R., Drory, N., Hopp, U., Snigula, J., Hill, G. J. 2003, *MNRAS*, 342, 605
- Fukugita, M., Shimasaku, K., Ichikawa, T. 1995, *PASP*, 107, 945
- Gilbank, D. G., Smail, I., Ivison, R. J., Packham, C., 2003, *MNRAS*, 346, 1125
- Gladders, M. D., Lopez-Cruz, O., Yee, H. K. C., & Kodama, A. 1998, *ApJ*, 501, 571
- Gomez, P., et al. 2003, *ApJ*, 584, 210
- Goto, T., Yamauchi, C., Fujita, Y., Okamura, S., Sekiguchi, M., Smail, I., Bernardi, M., Gomez, P. L. 2003a, *MNRAS*, 346, 601
- Goto, T., et al. 2003b, *PASJ*, 55, 757
- Hall, P. B., Green, R. F., Cohen, M. 1998, *ApJS*, 119, 1
- Henry, J. P. 2000, *ApJ*, 534, 565
- Hicks, A., Ellingson, E. 2006, in-prep
- Holden, B. P., et al. 2005, *ApJ*, 620, L83
- Holden, B. P., Stanford, S. A., Eisenhardt, P., Dickinson, M. 2004, *AJ*, 127, 2484
- Kochanek, C. S., White, M., Huchra, J., Macri, L., Jarrett, T. H., Schneider, S. E., Mader, J. 2003, *ApJ*, 585, 161
- Kochanek, C. S., et al. 2001, *ApJ*, 560, 566
- Kodama, T., Arimoto, N., Barger, A. J., Aragon-Salamanca, A. A. 1998, *A&A*, 334, 99
- Kodama, T., et al. 2004, *MNRAS*, 350, 1005
- Kodama, T., & Bower, R. 2003, *MNRAS*, 346, 1
- Lokas, E. L., & Mamon, G. A. 2001, *MNRAS*, 321, 155
- Lewis, I., et al. 2002, *MNRAS*, 334, 673
- Lewis, A. D., Ellingson, E., Morris, S. L., Carlberg, R. G. 1999, *ApJ*, 517, 587
- Lin, Y.-T., Mohr, J. J., & Stanford, S. A. 2004, *ApJ*, 610, 745 (L04)
- Lin, Y.-T., Mohr, J. J., & Stanford, S. A. 2003, *ApJ*, 591, 749
- Lopez-Cruz, O., Barkhouse, W. A., & Yee, H. K. C. 2004, *ApJ*, 614, 679
- Mannucci, F., Basile, F., Poggianti, B. M., Cimatti, A., Daddi, E., Pozzetti, L., Vanzi, L. 2001, *MNRAS*, 326, 745
- McCarthy, D., Ge, J., Hinz, J. L., Finn, R. A., de Jong, R. S. 2001, *PASP*, 113, 353
- Mushotzky, R. F., & Scharf, C. A. 1997, *ApJL*, 482, L13
- Muzzin, A., Yee, H. K. C., & Hall, P. B. 2006, submitted
- Navarro, J. F., Frenk, C. S., White, S. D. M. 1997, *ApJ*, 490, 493
- Nagai, D., & Kravtsov, A. 2005, *ApJ*, 618, 557
- Nelan, J. E., Smith, R. J., Hudson, M. J., Wegner, G. A., Lucey, J. R., Moore, S. A. W., Quinney, S. J., Suntzeff, N. B. 2005, *ApJ*, 632, 137
- Persson, S. E., Murphy, D. C., Krzemiński, W., Roth, M., Rieke, M. J. 1998, *AJ*, 116, 2475
- Poggianti, B. M. 1997, *A & AS*, 122, 399
- Postman, M., et al. 2005, *ApJ*, 623, 721
- Pozzetti, L., et al. 2003, *A&A*, 402, 837
- Press, W. H., Teukolsky, S. A., Vetterling, W. T., Flannery, B. P. 1992, *Numerical Recipes in Fortran 77, Vol 1; Second Edition*; Cambridge, Cambridge University Press
- Ramella, M., Boschin, W., Geller, M. J., Mahdavi, A., Rines, K. 2004, *AJ*, 128, 2022
- Rines, K., Geller, M. J., Diaferio, A., Kurtz, M. J., Jarrett, T. H. 2004, *AJ*, 128, 1078 (R04)
- Rix, H.-W., Rieke, M. J. 1993, *ApJ*, 418, 123
- Sand, D. J., Treu, T., Smith, G. P., & Ellis R. S. 2004, *ApJ*, 604, 88
- Schlegel, D. J., Finkbeiner, D. P., & Davis, M. 1998, *ApJ*, 500, 525
- Schechter, P. 1976, *ApJ*, 203, 297
- Shectman, S. A., Landy, S. D., Oemler, A., Tucker, D. L., Lin, H., Kirshner, R. P., Schechter, P. L. 1996, *ApJ*, 470, 172
- Skrutskie, M. F., et al. 2006, *AJ*, 131, 1163
- Smith, G. P., Treu, T., Ellis, R. S., Moran, S. M., Dressler, A. 2005, *ApJ*, 620, 78
- Stanford, S. A., Eisenhardt, P. R., & Dickinson, M. 1998, *ApJ*, 491, 461
- Stanford, S. A., Eisenhardt, P. R., Dickinson, M., Holden, B. P., de Propris, R. 2002, *ApJS*, 142, 153 (SED02)
- Strazzullo, V., et al. 2006, *A&A*, 450, 909
- Tanaka, M., Kodama, T., Arimoto, N., Okamura, S., Umetsu, K., Shimasaki, K., Tanaka, I., Yamada, T. 2005, *MNRAS*, 362, 268
- Tanaka, M., Goto, T., Okamura, S., Shimasaku, K., Brinkmann, J. 2004, *AJ*, 128, 2677
- Toft, S., Mainieri, V., Rosati, P., Lidman, C., Demarco, R., Nonino, M., Stanford, S. A. 2004, *A&A*, 422, 29
- Tokunaga, A. T., Simons, D. A., Vacca, W. D. 2002, *PASP*, 114, 180
- Tran, K.-V., van Dokkum, P., Franx, M., Illingworth, G. D., Kelson, D. D., Schreiber, N. M. F. 2005, *ApJ*, 627, L25
- Treu, T., et al. 2003, *ApJ*, 591, 53
- Valdes, F. 1982, *Proc SPIE*, 331, 435
- van der Marel, R. P., Magorrian, J., Carlberg, R. G., Yee, H. K. C., Ellingson, E. 2000, *AJ*, 119, 2038
- van Dokkum, P. G., & Stanford, S. A. 2003, *ApJ*, 585, 78
- van Dokkum, P. G., Franx, M., Kelson, D. D., Illingworth, G. D. 2001, *ApJ*, 553, 39
- van Dokkum, P. G., Franx, M., Fabricant, D., Kelson, D. D., Illingworth, G. D. 1999, *ApJ*, 520, L95
- van Dokkum, P. G., Franx, M., Kelson, D. D., Illingworth, G. 1998, *ApJ*, 504, L17
- Wechsler, R. H., Bullock, J. S., Primack, J. R., Kravtsov, A. V., Dekel, A. 2002, *ApJ*, 568, 52
- Yee, H. K. C., & Ellingson, E. 2003, *ApJ*, 585, 215
- Yee, H. K. C., et al. 2000, *ApJS*, 129, 475
- Yee, H. K. C., Ellingson, E., Morris, S. L., Abraham, R. G., Carlberg, R. G. 1998, *ApJS*, 116, 211
- Yee, H. K. C., Ellingson, E., & Carlberg, R. G. 1996a, *ApJS*, 102, 269
- Yee, H. K. C., Ellingson, E., Abraham, R. G., Gravel, P., Carlberg, R. G., Smecker-Hane, T. A., Schade, D., Rigler, M. 1996b, *ApJS*, 102, 289
- Yee, H. K. C. 1991, *PASP*, 103, 662

TABLE 1
SUMMARY OF OBSERVATIONAL DATA FOR THE CNOC1 CLUSTER SAMPLE

Cluster	z	N_{spec} ($R \leq R_{200}$)	K_{lim} (mag)	Seeing ($''$)	g/r area (\square')	K area (\square')	MOS Fields	% R_{200} Obs
(1)	(2)	(3)	(4)	(5)	(6)	(7)	(8)	(9)
A2390	0.2279	140	18.08	1.2	269.56	249.01	5×1	60.9
MS0016+16	0.5466	52	18.57	1.1	57.58	57.58	1×1	100.0
MS0302+16	0.4246	26	19.12	0.9	63.27	62.62	1×1	100.0
MS0440+02	0.1965	33	19.01	1.4	182.02	168.46	3×1	89.0
MS0451+02	0.2010	76	18.66	0.9	253.41	173.75	4×1	53.6
MS0451-03	0.5392	64	18.69	0.9	61.22	61.22	1×1	100.0
MS0839+29	0.1928	39	18.70	0.9	176.35	167.47	3×1	68.3
MS1006+12	0.2605	29	18.14	0.9	59.13	57.51	1×1	81.0
MS1008-12	0.3062	61	17.89	1.0	63.01	45.29	1×1	73.1
MS1224+20	0.3255	29	18.05	0.8	57.07	71.72	1×1	93.5
MS1231+15	0.2350	67	18.66	0.9	181.35	181.35	1×3	100.0
MS1358+62	0.3290	136	17.93	1.2	193.71	185.14	1×3	100.0
MS1455+22	0.2570	57	18.22	0.9	58.69	56.39	1×1	77.3
MS1512+36	0.3726	23	18.75	1.0	207.61	181.45	3×1	100.0
MS1621+26	0.4274	59	18.85	1.1	72.44	67.72	1×1	100.0

NOTE. — (3) Number of spectroscopic clusters members with $R \leq R_{200}$, (4) 5σ limiting magnitude of observations, (6) Total area with g and r band data, (7) Total area with both K-band and g/r data (9) Percentage of a circle with radius R_{200} with K-band imaging

TABLE 2
COMPARISON OF 2MASS AND CNOC1 PHOTOMETRIC
ZEROPOINTS

Cluster (1)	N_{stars} (2)	$K_{CNOC}-K_{2MASS}$ (3)
A2390	70	0.042 ± 0.045
MS0016+16	7	0.180 ± 0.038
MS0302+16	9	0.003 ± 0.052
MS0440+02	62	0.064 ± 0.015
MS0451+02	43	0.005 ± 0.030
MS0451-03	15	0.058 ± 0.038
MS0839+29	27	0.025 ± 0.028
MS1006+12	7	0.048 ± 0.058
MS1008-12	6	-0.003 ± 0.080
MS1224+20	7	0.009 ± 0.043
MS1231+15	9	-0.068 ± 0.079
MS1358+62	23	-0.043 ± 0.043
MS1455+22	6	0.117 ± 0.079
MS1512+36	18	-0.097 ± 0.051
MS1621+26	20	0.114 ± 0.084

TABLE 3
SUMMARY OF LF PARAMETERS

Redshift (1)	Type (2)	Environment (3)	K* (4)	α (5)
0.296	all	-	-24.53±0.15	-0.84 ±0.08
"	all	-	-24.93±0.04	-1.1
"	ELL	-	-24.09±0.14	0.17 ± 0.18
"	EM+BAL	-	-24.27±0.27	-0.95 ± 0.27
0.210	all	-	15.52±0.06	-0.9
"	ELL	-	16.17±0.06	0.2
"	EM+BAL	-	16.06±0.12	-0.9
0.290	all	-	15.93±0.06	-0.9
"	ELL	-	16.72±0.07	0.2
"	EM+BAL	-	16.12±0.18	-0.9
0.462	all	-	17.14±0.06	-0.9
"	ELL	-	17.44±0.06	0.2
"	EM+BAL	-	17.20±0.14	-0.9
0.296	all	Cluster-Low Mass	-24.51±0.08	-0.9
"	ELL	"	-23.94±0.08	0.2
"	EM+BAL	"	-23.85±0.17	-0.9
"	all	Cluster-Mid Mass	-24.59±0.06	-0.9
"	ELL	"	-23.99±0.05	0.2
"	EM+BAL	"	-24.08±0.14	-0.9
"	all	Cluster-High Mass	-24.52±0.06	-0.9
"	ELL	"	-24.10±0.05	0.2
"	EM+BAL	"	-23.72±0.09	-0.9